University of Central Florida

STARS

2021

Fluid-Structure Interaction for a Deformable Anisotropic Cylinder: A Case Study

Jared T. Decker
University of Central Florida

Recommended Citation

FLUID-STRUCTURE INTERACTION FOR A DEFORMABLE ANISOTROPIC
CYLINDER: A CASE STUDY

by

JARED T. DECKER

A thesis submitted in partial fulfillment of the requirements
for the Honors Undergraduate Thesis Program
in the Department of Mechanical and Aerospace Engineering
in the College of Engineering and Computer Science
at the University of Central Florida
Orlando, Florida

Summer Term
2021

Thesis Chair: Luigi E. Perotti

I Abstract

For a structure designed to interact with the surrounding fluid, structural deformation under loads induced by fluid flows is an important factor to consider, and one which is traditionally difficult to account for analytically. Coupling the finite element method for structural analysis with the finite volume method for the determination of fluid response allows for accurate simulation of the pressure and shearing loads applied by the fluid onto the fluid-structure interface, while also determining localized structural displacements that would cause changes to the geometry of the interface. This work seeks to simulate the behavior of cylinders with varying heights and stiffnesses under external flows with low Reynolds numbers. To address structural deformation accurately in the simulation, a morphing and remapping algorithm is applied to the fluid-structure interface. With additional consideration for anisotropy in the structure's elasticity, these analyses could potentially support the development of flexible components that deform in predetermined ways under anticipated fluid loads, allowing for simpler and more efficient solutions to control flow scenarios that traditionally require moving components and control surfaces.

Contents

List of Figures

List of Tables

II Introduction

Fluid flows interact with their surroundings, applying both pressures and shear stresses to any object immersed in the flow. The impact of a physical object on the surrounding fluid flow can be determined through computational fluid dynamics (CFD) simulations. However, unless the object is modeled as a deformable solid, CFD simulations do not directly address the fluid flow's impact on the structure's deformation. On the other hand, solid mechanics has long been used to analytically model the behavior of a structure under applied load and displacement boundary conditions, and these behaviors can be modeled numerically using the finite element method (FEM). However, just as CFD modeling does not consider the deformation of immersed objects, structural modeling alone cannot represent the impact of deforming solids on a surrounding fluid flow. Merging of fluid and structural modeling yields simulations of fluid-structure interaction, the goal of which is to simultaneously simulate fluid and structural behavior, and accurately simulate how the fluid and solid domains impact one another when a deformable structure is submerged into a fluid flow [1].

Anisotropic materials have been in use for centuries [2]. With the advances in material science and numerical modeling capabilities, material anisotropy is leveraged in modern engineering applications to control deformation and structural response under given loads. The application of intentional anisotropic behavior in response to fluid flow conditions could prove valuable, potentially allowing for novel design concepts that would not be feasible with traditional isotropic materials, in fields ranging from medicine [3, 4] to aeronautics [5] and beyond.

II.1 Fluid Modeling

The Finite Volume Method (FVM) solves the governing equations in fluid dynamics over a user-defined spatial domain. Like in many numerical methods, the fluid domain is first discretized into subdomains, or cells, forming a mesh [6, 7, 8]. While too coarse meshes

will not yield accurate results, too refined meshes may require a prohibitive computational cost to yield any results [6, 7, 8, 9], so mesh refinement studies should be carried out to balance solution accuracy against computational cost. Multiple approaches to meshing a domain exist. Polygonal meshes are a newer approach to meshing with promising abilities to handle complex geometries, but can potentially have compatibility issues when attempting to interface with other solvers [7]. Of better-known fluid meshing approaches, two primary mesh types exist: tetrahedral meshes and hexahedral meshes [8]. Of these, tetrahedral meshes are better able to represent complex geometries, but they are prone to developing quality issues like cell warping that must be avoided, as such quality issues reduce solution accuracy [7, 8]. For a tetrahedral cell to provide accurate results, one should strive for an aspect ratio close to one, meaning all edges of a cell are close to equal in length [8]. Hexahedral meshes are more resistant to warping and other quality issues, but accurately representing complex geometries using only hexahedral cells is challenging [7, 8], and can result in meshes being too fine to yield results at a reasonable computational cost [6, 7]. Polyhedral meshes, which do not have a fixed number of faces on each cell, seek to address the problems presented by both tetrahedral meshes and hexahedral meshes by allowing a mesh to be resistant to warping while also representing complex geometry in a more efficient manner than hexahedral cells.

For many liquids, factors like density and viscosity are treated as constant, making them incompressible Newtonian fluids. However, compressible fluids, like gases traveling at high speeds [6, 7] can also be modeled with modifications made to the governing equations chosen to account for the changes in density. Additionally, non-Newtonian fluids, such as power-law fluids [10] can also be modeled, provided the viscous behavior is properly defined.

The behavior of a low-speed incompressble flow about a circular cylinder is an interesting case to study, due in part to its tendency to never achieve a steady state [7, 9, 11, 12], instead shedding oscillating vortices downstream of the cylinder. These oscillating vortices also generate alternating lift forces on the cylinder [9, 12], which can cause vibrations [9]

and, if the cylinder is treated as flexible, oscillating structural deformation. The tendency to shed oscillating vortices about a cylinder at low Reynolds numbers has also been simulated for power-law fluids [13]. Wind tunnel tests have determined that the vortex shedding phenomenon can also occur at much higher Reynolds numbers, near $Re = 10^7$ [14], and that cylinders with higher aspect ratios, or more significant heights relative to their diameters, sometimes switch between the expected vortex shedding phenomenon and a more unpredictable 'irregular flow' [15] that erratically changes its direction and never settles to a 'steady state'.

Because the cylinder in low-speed flow exhibits specific and unique characteristics, it is often used as a validation case for fluid simulations, like FVM solvers [7].

II.2   Structural Modeling

When loaded, a structure deforms to some extent [16] as a function of the properties of the material and the geometry of the structure. For many common materials in engineering [2, 3, 16], material properties are considered independent of orientation. Such materials are isotropic.

Anisotropic materials, with properties that vary by material orientation, have been used for centuries [2]. Intentional use of anisotropy in design is a somewhat newer concept [3, 5], although it does have promising applications. Fibrous composites often have significant anisotropy in their strength and other properties, typically aligned with the internal grains and fibers [17, 18], while biological materials often exhibit both anisotropic and non-linear elastic behavior [4, 19].

The Finite Element Method (FEM) is frequently used to model the response of a structure. As in the FVM, the FEM requires that a structure is first discretized into smaller cells called elements, which then are used as the spatial basis for calculations of displacements

3

and corresponding stresses and strains [20].

As in the FVM, finer meshes offer greater potential accuracy, but require more computational cost and time to provide results. FEM meshes that are too coarse will produce less accurate results. Again, a mesh refinement study must be carried out to optimize the balance of accuracy and cost. Multiple options for meshing exist, with a variety of different approaches for different scenarios. Specialized beam and shell elements can be used when applicable [20], as well as elements intended for generalized 3-D stress simulations. Of the latter category, typical elements' types include tetrahedra and hexahedra, as seen in Fig. 1.

Linear Tetrahedral Element (4 nodes)　　　　Linear Hexahedral Element (8 nodes)

Quadratic Tetrahedral Element (10 nodes)　　　Quadratic Hexahedral Element (20 nodes)
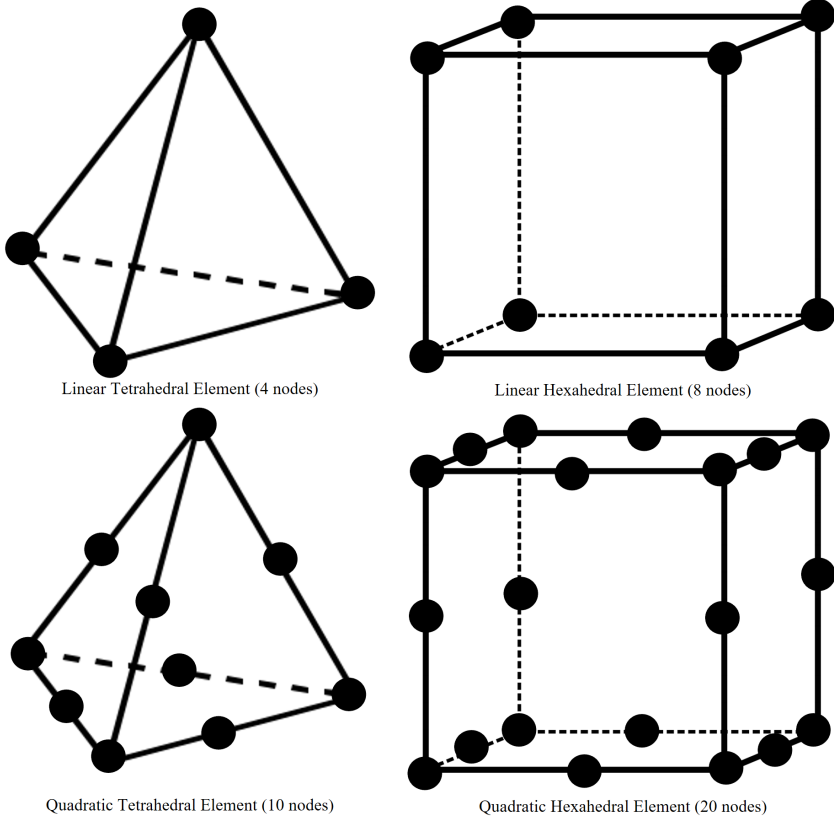
Figure 1: Common Element types in Finite Element Analysis

II.3 Flow-Induced Structural Vibrations

At low Reynolds numbers, alternating vortices are shed in the wake of a structure submerged in a flow. The result of this vortex shedding is alternating loads on the structure, which can cause vibrations [9, 21, 22, 23] in addition to structural deformation. Referred to generally as vortex-induced vibrations, these behaviors can become an important load to consider in the design process for some mechanisms and devices, as these vibrations may have unwanted side effects, such as noise. The alternation of loads can also become a driving factor behind premature fatigue failure.

The shape of the structure in question can have significant impacts on its dynamic characteristics. While a single cylinder in crossflow might oscillate in a reasonably steady manner, particularly if constrained by a spring and damper [9], a structure with a square cross-section instead 'gallops', with much more aggressive and unpredictable motion [21]. Cylinders placed near one another will respond differently as well, since the wakes of each cylinder will impact those downstream or to the sides [22, 23].

A vibrating cylinder can impact its own wake as well, and if the amplitude of the vibrations grows large enough [24], due to a 'locking-in' phenomenon, this violent vibration and wake oscillation can eventually become less dependent on flow speed.

II.4 Fluid-Structure Interaction with Isotropic Linear-Elastic Structures

Fluid loads cause structural deformation just as readily as any other load source [16], and as such, FSI simulations have proven helpful in preventing structural and product failures. Oil and natural gas wells are exposed to internal fluid loads [25] due to fluid flow through their pipes, pumps and other components, although external fluid loads may also exist when drilling offshore [25, 26] due to currents and waves present offshore.

When a flexible thin plate is attached on the downstream side of a cylinder or other bluff body, it is expected to oscillate much like the vortices behind a cylinder do in fluid simulations that neglect structural deformation. This behavior resembles that of a flag blowing in the wind, a common everyday occurrence that can be observed easily, and as a result, this 'flag' test is frequently used as a validation case for FSI solvers and solutions [1, 27, 28].

II.5 Fluid-Structure Interaction with Anisotropic and Nonlinear Structures

When considering large structural displacements, like those characteristic of nonlinear materials, different numerical methods are likely to become necessary. While different means for managing such large displacements exist, the fluid and structural simulations must be tightly coupled [1, 29, 30, 31]. One common method is the use of Arbitrary Legrangian-Eulerian (ALE) FSI algorithms, which assist in bridging the gaps between the Lagrangian reference-frame based calculations used in structural analysis [16] with the fixed Eulerian spatially-defined configuration favored in fluid mechanics [30]. Additionally, when large deformations are present, care must be taken to ensure the meshed fluid and solid domains are able to properly interact, often requiring either overset grids [29, 30, 31] or the application of a mesh morphing algorithm [7, 32].

Anisotropic material, like carbon fiber, has potential uses in the context of fluid interaction. Changing the alignment of internal fibers, as expected, changes the material's strength along a given direction [17, 18]. If arranged into a fluid-filled tube where the fluid is subjected to a shock wave, the speed at which the waves travel is impacted by the angle of the preferential orientation [17].

In biology and medicine, arterial walls have been modeled as nonlinear anisotropic material, shaped as a tube, with loads coming from the internal flow [4]. The orientation of

implanted meshes and filters made of biologically-safe polymers also has significant implications on the longevity and effectiveness of the device [3], and simulation results suggested the orientation is dictated by the material anisotropy of the mesh and the nonlinearity of the polymers in use. The heart has been the subject of extensive FSI modeling, and FSI simulations have helped model the dynamics and mechanics of natural heart valves, mechanical valves, and polymeric valves [19], with promising results when compared against *in-vivo* valve kinematics that could help drive the design of future replacement heart valves.

III   Methods

The objective in this research is to model fluid-structure interaction for cylinders of varying aspect ratios and different material properties in crossflow, under low-velocity laminar flows.

III.1   Fluid Analysis

For this work, an incompressible laminar flow is selected. Most liquids are incompressible [7], and their densities ρ_{fluid} are constant, independent of flow velocity. A fluid flow is defined as laminar or turbulent based on the Reynolds number Re, which represents the ratio of inertial to viscous forces in a fluid flow, as defined below:

$$Re = \frac{uL}{\nu} = \frac{\rho u L}{\mu}\,, \tag{1}$$

where u is the flow velocity, L is the characteristic length, e.g., the diameter of the cylinder in cross flow, and ν is the kinematic viscosity. Alternatively, the kinematic viscosity can be replaced by the dynamic viscosity $\mu = \nu/\rho$. When considering the impacts of the fluid flow on a surface, the benefits of using the dynamic viscosity are readily apparent, as μ is used to relate fluid strain rate $\dot{\gamma}$ to the shear stress τ with Newton's Law of Viscosity:

$$\tau = \mu\dot{\gamma}\,, \tag{2}$$

where the fluid's shear strain rate $\dot{\gamma}$ is defined as the partial derivative of fluid velocity u parallel to the surface with respect to distance from the surface y, or $\dot{\gamma} = \frac{\partial u}{\partial y}$. For this work, Newtonian fluids are the focus, meaning the dynamic viscosity μ is constant, independent of the shear strain rate $\dot{\gamma}$ and shear stress τ, although many other fluids are non-Newtonian, like the power-law fluids [10] found frequently in nature.

Considering a steady, incompressible flow, and neglecting the viscous effects present to

some extent in all flows, the Bernoulli equation can be used to relate a variety of fluid parameters at any arbitrarily selected point along a given streamline in the fluid:

$$P + \frac{1}{2}\rho v^2 + \rho g z = \text{constant} \,, \tag{3}$$

where static pressure P and dynamic pressure $\frac{1}{2}\rho v^2$ can be summed to obtain the constant stagnation pressure P_0, while $\rho g z$ accounts for the weight of the fluid above the streamline on which Bernoulli's equation is used. Bernoulli's equation is straightforward to calculate, making it well-suited for quick estimations of fluid behavior using minimal computational resources [6]. However, the Bernoulli equation is not suited for any cases where flows become compressible, like air at high speeds [7], or for cases where viscous forces are expected to have significant impact, like the creeping flows with low Reynolds number which are the focus of this work. For cases where viscosity plays a significant role, the Navier-Stokes equations are better suited for numerically modeling fluid behavior. For viscous and incompressible flows, the Navier-Stokes equation takes the form:

$$\rho \frac{D\vec{v}}{dt} = -\vec{\nabla} P + \mu \nabla^2 \vec{v} + \rho g \,, \tag{4}$$

where ρ is the fluid density, $\vec{v}$ is the fluid velocity vector, t represents time, P is the pressure, μ is the dynamic viscosity, and g is the gravitational acceleration.

When a cylinder is submerged in a creeping flow with a sufficiently low Re, clearly-defined vortices will be shed in the cylinder's wake, with the generation of the vortices alternating from one side of the cylinder to another. As this study will be utilizing such creeping flows, vortex shedding frequency f should not only be easily determined, but may also be impacted by the FSI conditions, due to the deformation of the cylinder under the fluid loads. Vortex shedding frequency f is governed by the Strouhal number St, as shown in Eq. (5):

9

$$St = \frac{fd}{u} = f(Re) \tag{5}$$

The Strouhal number St governs the relation between vortex shedding frequency f, cylinder diameter d, and flow speed u. Additionally, St is a function of the Reynolds number Re. Vortex shedding frequency can be determined both by the relation in Eq. (5) and by observing the alternating direction of force components perpendicular to the flow (lift) on the cylinder.

III.1.1 Finite Volume Method

Computational Fluid Dynamics (CFD) calculations are carried out using the Finite Volume Method (FVM) in the Star-CCM+ commercial simulation software [32]. A domain is defined to represent the fluid flow around the structure of interest. This domain is then discretized into a hybrid hexahedral-polyhedral mesh, with high refinement near the fluid-structure interface, and coarser cells further away from the surface, as shown in Fig. 2.

Once the fluid domain is meshed, the FVM solver provided by Star-CCM+ solves the Navier-Stokes equations, defined earlier in Eq. (4), in each cell of the fluid domain mesh by iteration.

As the flow develops over time without reaching a steady state regime, an implicit unsteady solver is chosen to determine the transient flow behavior. Star-CCM+'s second-order temporal discretization will also be utilized to aid in solution accuracy and stability [32]. The simulation time and timestep parameters in Table 1 have been selected for preliminary testing.

Table 1: Solver temporal parameters for the FVM solution

Simulated Time	10 s	# Timesteps	10 000
Timestep Duration Δt	0.001 s	Internal Iterations	100 per timestep

In unsteady solutions, the number of internal iterations selected is crucial to the accuracy of the solution. While this is true of all unsteady solvers, this is especially important in Star-CCM+, as rather than determining when to proceed to the next timestep based on meeting user-defined residual and convergence criteria, Star-CCM+ carries out all of the allotted internal iterations per timestep [7]. This is believed to produce more accurate results, albeit at the expense of computational resources [6]. Likewise, the Δt covered by a timestep should be small enough to accurately represent the flow's behavior. While 'rules of thumb' exist, particularly in commercial applications, the duration selected here has previously been shown to accurately represent the fluid behavior in CFD simulations of a cylinder in crossflow, provided the mesh was sufficiently refined [9].
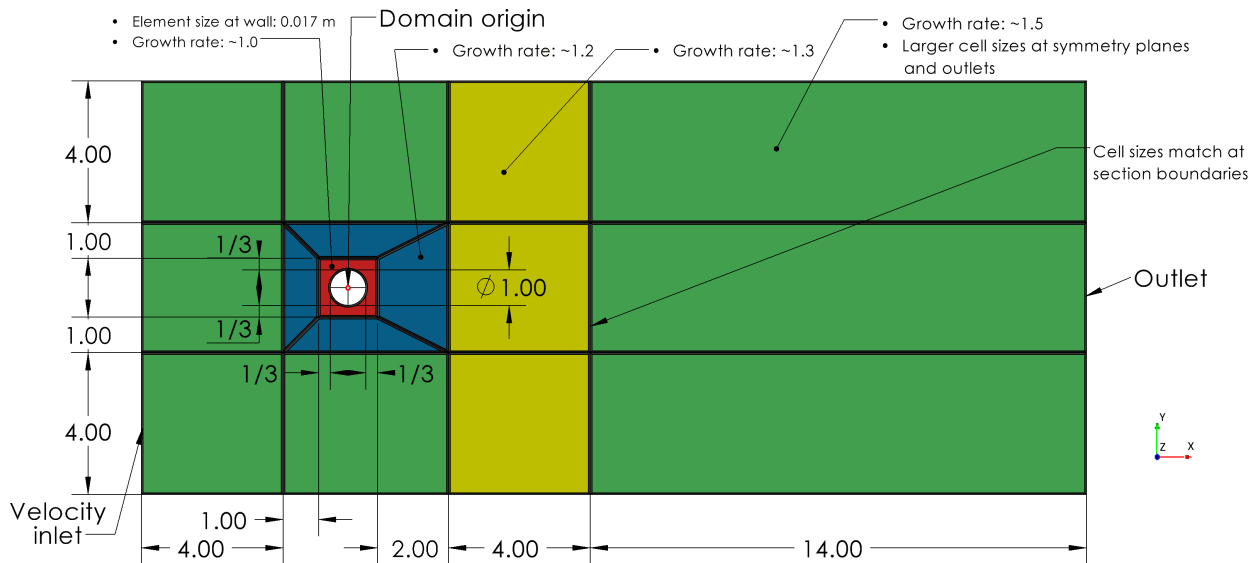
Figure 2: Fluid domain overview, featuring key dimensions and mesh refinement criteria. Coordinate axes are included for reference, but the origin is located in the center of the cylinder. Dimensions are given in meters.

In most simulations, including CFD, mesh quality impacts the accuracy of the results [1, 6, 7, 8, 9]. As for the timestep and iteration parameters, a balance must often be found between maximizing accuracy and achieving acceptable computational time. Finer meshes

11

may lead to greater accuracy, but at great computational cost. Targeted refinement in key areas of the mesh, as seen in Fig. 2 is a crucial tool to balancing cost with accuracy, as having a finer mesh near the areas where fluid activity is of the greatest interest will improve accuracy, and if the areas further from the surface are kept coarser, the improved accuracy comes at a reduced cost. In this work, the mesh will be most refined near the cylindrical surface that acts as the fluid-structure interface. Farther from the interface the mesh can be coarsened with significant coarsening near the edges of the domain. Additionally, care must be taken to ensure the domain is sized such that there is acceptable distance between the surfaces which are defined as inlets, outlets, and symmetry planes, and the surfaces which become the interface between fluid and structure. As seen in Fig. 2, the cylinder is placed at significant distance from the edges of the domain, roughly $5 \times d_{\text{cylinder}}$ at minimum. The top of the cylinder is submerged, with 1 m of fluid domain above the top surface of the cylinder.

III.1.2   Boundary Conditions in the Fluid Domain

Assigning boundary conditions in the fluid domain requires the definition of surfaces that are designated as either inlets, outlets, walls, or symmetry planes. For the simulation described in this work, a velocity inlet is selected and placed on the 'left' or negative-x face. The outlet is placed opposite to the inlet on the 'right' or positive-x face. The other surfaces surrounding the domain (the surfaces with normals along the $\pm\mathbf{e}_y$ and $\pm\mathbf{e}_z$ directions as seen in Fig. 2), are defined as symmetry planes, while all surfaces corresponding to the cylinder, including the circular top face, are defined as walls with a non-slip condition, meaning the fluid velocity at the surface is zero. Based on a creeping, low-Reynolds number target, the parameters outlined in Table 2 are applied to the simulation.

The viscosity selected resembles that of plant-based oils like sunflower oil, although the density more closely resembles that of air or other gases than liquids. These parameters are chosen to achieve a low Re.

Table 2: Fluid flow parameters

Initial Fluid Velocity [x,y,z]	[0.0, 0.0, 0.0] m/s	Inlet Velocity [x,y,z]	[25.0, 0.0, 0.0] m/s
Fluid Density ρ_{fluid}	1.0 kg/m^3	Dynamic Viscosity μ	0.05 Pa-s
Targeted Reynolds Number Re	500	Characteristic Length L	1.0 m

III.2 Structural Analysis

Material selection is a critical part of the engineering design process [16]. For many common materials, material properties like Young's modulus and density are independent of orientation [5, 16], or can be approximated as such [2]; these materials are referred to as isotropic. Alternately, anisotropic materials, like some textiles [5] and carbon fiber composites [18], have material properties that vary with orientation, and the material anisotropy must be accounted for in the design process [3, 5].

In the infinitesimal strain regime, most material behave as linearly elastic and Hooke's law is chosen to describe their elastic behavior:

$$\boldsymbol{\sigma} = \boldsymbol{C} : \boldsymbol{\epsilon}, \tag{6}$$

where the stress tensor $\boldsymbol{\sigma}$ is linearly proportional to the strain tensor $\boldsymbol{\epsilon}$ via the elasticity tensor $\boldsymbol{C}$.

III.2.1 Finite Element Method

The finite element method (FEM) enables computational analysis of solid mechanics, much as the FVM is the common numerical method used in CFD analyses. For simplicity, in this work, Star-CCM+ will also be adopted as the FEM solver. This presents the advantage that all coupling and mapping between the fluid and solid domains are implemented in the same software environment [32]. However, as part of testing and validating the presented analyses, Star-CCM+'s FEM solver has been compared to the FEM solver in the industry-standard FEA software Abaqus [20], as well as analytical solutions, when available, and the differences

in benchmark simulations were minimal. Like in the FVM, the structure, represented as a solid domain, must be discretized into a mesh.

In this work, the linear elastic cylinder is discretized using the quadratic hexahedral elements seen in Fig. 1, as shown in Fig. 3, with an average element length of roughly 0.125 m.

(a) Base View   (b) Isometric View   (c) Side View
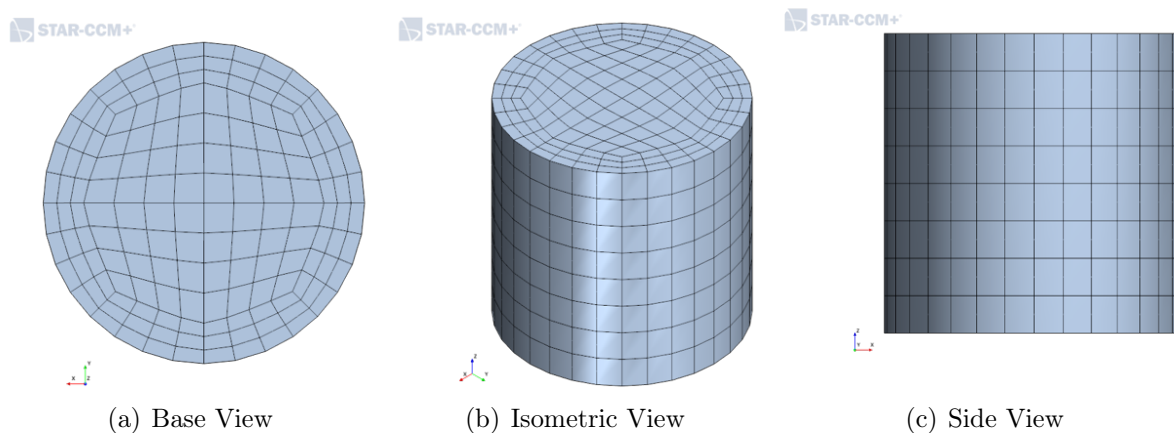
Figure 3: Cylinder mesh selected for study, shown for $h_{\text{cyl}} = 1.0$ m.

For a linear elastic solid as the one considered herein, after assembling, the FEM equations at the model level can be summarized as:

$$M\ddot{U} + C\dot{U} + KU = F, \tag{7}$$

where M is the mass matrix, U are the unknown nodal displacements to be computed, C is the damping matrix, K is the stiffness matrix, and F represents the nodal forces.

In order to eliminate rigid body motions, the bottom (with normal $-\mathbf{e}_z$) surface of the cylinder is fully constrained.

III.3   Modulating the Fluid-Structure Interaction

The goal of the current study is to investigate the impact of the structural response on the fluid flow and vice-versa. We will consider four aspect ratios (Table 3) and three Young's moduli. The cylinder's aspect ratio $h_{\mathrm{cyl}}/d_{\mathrm{cyl}}$ will be altered by modifying the cylinder height while keeping its diameter constant. This will allow consideration of a shear-dominant versus a bending-dominant response.

Table 3: Cylinder aspect ratios, heights, and dominant structural response

Aspect Ratio $h_{\mathrm{cyl}} : d_{\mathrm{cyl}}$	Cylinder Height h_{cyl} (m)	Dominant Loading
0.5 : 1	0.5	Shearing
1 : 1	1.0	
5: 1	5.0	Some Bending & Shearing

In addition, multiple material cases will be considered here, including isotropic linear-elastic materials as a baseline case, as well as materials with an anisotropic elastic response due, for example, to the presence of fibers along a preferential direction. Table 4 lists the current material properties that have been chosen for this research.

Table 4: Selected structural material properties

Material Law	Case	Material Properties		
Isotropic	Near-Rigid	$E = 100$ GPa	$\nu = 0.3$	$\rho = 2500$ kg/m^3
	Mid-Range	$E = 100$ MPa	$\nu = 0.3$	$\rho = 2500$ kg/m^3
	Softest	$E = 100$ kPa	$\nu = 0.3$	$\rho = 2500$ kg/m^3
Anisotropic	Preferential Angle $\psi = 45°$	$E_{\mathrm{fiber}} = 1$ GPa	$\nu_{\mathrm{fiber}} = 0.25$	$\rho_{\mathrm{fiber}} = 2500$ kg/m^3
	Fiber Volume % = 60	$E_{\mathrm{matrix}} = 10$ MPa	$\nu_{\mathrm{matrix}} = 0.3$	$\rho_{\mathrm{matrix}} = 1000$ kg/m^3

For the softest isotropic material, a load-stepping algorithm [32] may be employed to stabilize the finite element simulation and account for potential nonlinear behavior.

III.4   FSI Coupling

This simulation is an implicit-unsteady simulation, with two-way coupling implemented internally in Star-CCM+ [32]. The two-way coupling process is computationally intensive.

Mapping FVM cells to FEM elements and surfaces, or finding the surfaces of the FVM mesh that best correspond to their FEM counterparts, and vice-versa, is often the most difficult and demanding component of the simulation [7]. As seen in Fig. 4, the FSI coupling reduces to essentially two operations: 1) the mapping of pressures and shears, or traction vectors, from the FVM simulation to the appropriate FEM elements or nodes; and 2) the mapping of FEM nodal displacements to displacements of the FVM mesh's vertices, which also requires mesh 'morphing' or remeshing to occur. However, when using mesh morphers, the risk of creating 'negative-volume' or 'zero-volume' cells may present itself [7], especially when dealing with high displacements and structural velocities. In these cases, application of an overset mesh is a more reliable and accurate approach [1, 30], but these unstable structural behaviors are not anticipated based on the fluid loads selected in this study.

Traction Vectors

• Pressure, shear stress
• Map FVM-generated loads to FEM surfaces

FVM Solver

FEM Solver

Nodal Displacements

• Remeshing
• Map FEM displacements to FVM mesh vertices
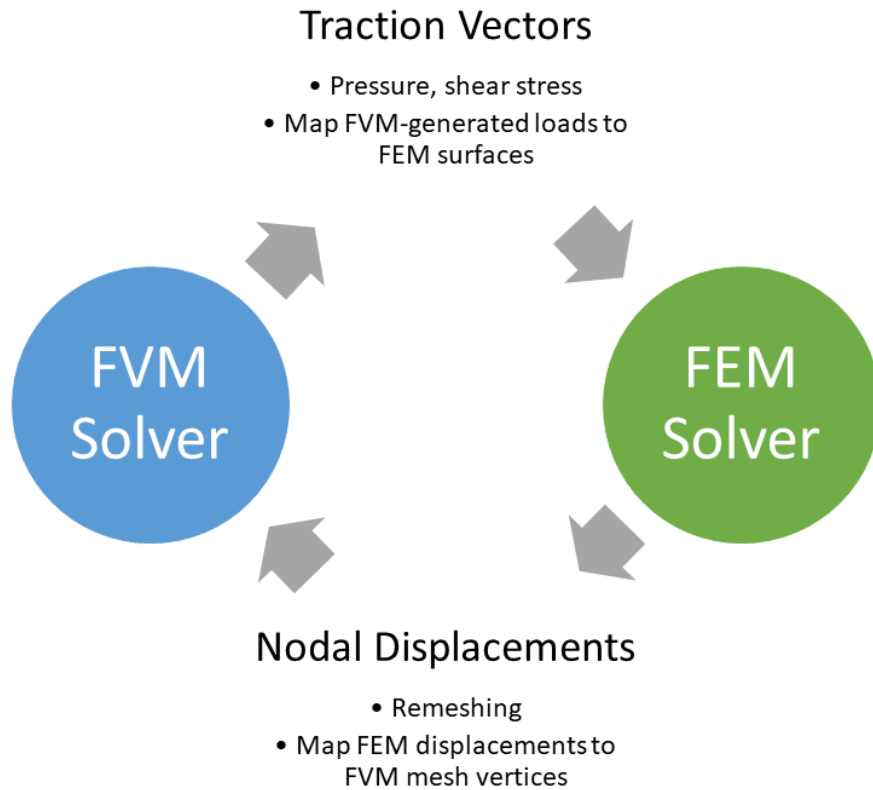
Figure 4: Overview of the implicit coupling process for FSI simulations.

The processes and steps outlined in Fig. 4 are repeated and iterated several times in each

timestep, to ensure the fluid and solid domains interact correctly and prevent mid-timestep mapping failures.

The coupled simulation also requires clear definition of the FSI interface and its motion. The FSI interface is defined on the 'wetted surface' of the structure, or the portion where the fluid loads are applied, and then its movement is set to match the FEM nodal displacements [7], which will update automatically throughout the simulation. No rigid-body translations or rotations are prescribed to the FSI interface, as these behaviors should not occur based on the structural boundary conditions. Once the interface's motion is determined, Star-CCM+'s mesh morphing algorithm [32] remeshes the fluid domain, ensuring that the fluid mesh cells and vertices continue to properly map to the FEM nodes and elements after the movement of the FSI interface.

IV Method Validation & Mesh Refinement Study

Prior to carrying out fully-coupled FSI numerical analyses, the methods involved, like the FEM and FVM implementations, must be verified independently [1]. Additionally, mesh refinement studies should be carried out. Once these steps are complete, the simulations can proceed.

IV.1 Verification of Fluid Analysis

For a cylinder in crossflow at low Reynolds numbers, the 'vortex shedding' phenomenon is a well-documented and studied verification method [7, 9]. If the simulation is set up correctly, vortices should be shed at a predictable rate once the simulated flow has developed. To test this, preliminary CFD simulations are carried out in Star-CCM+ [32] to verify the accuracy of the solver. As this is a validation case that was used to develop and validate Star-CCM+ [7, 32], the outcome of this validation case should be accurate. Visually, these vortices are seen shedding in the wake of the cylinder, shown in Fig. 5.
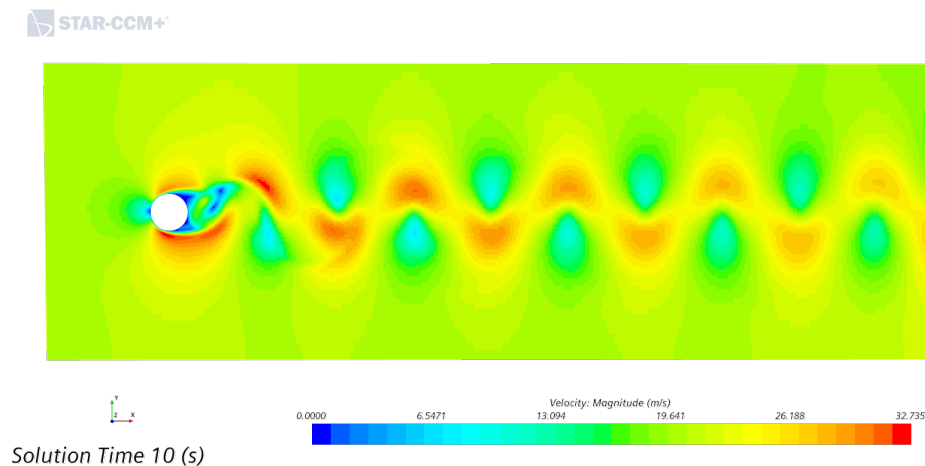

Figure 5: CFD simulation of a cylinder in crossflow shows clearly-defined vortices shedding in the wake region when flow velocity is plotted.

Plots of lift and drag force on the cylinder assist in the numerical observation of the vortex shedding phenomenon. The oscillation should be regular, appearing almost sinusoidal, as

seen in Fig. 6. When the lift crosses zero, the vortex shedding has alternated to the opposite side of the cylinder. In a physical case, this would mean the cylinder is first pushed 'up', then 'down', then back up again, oscillating with the vortices shed [9].
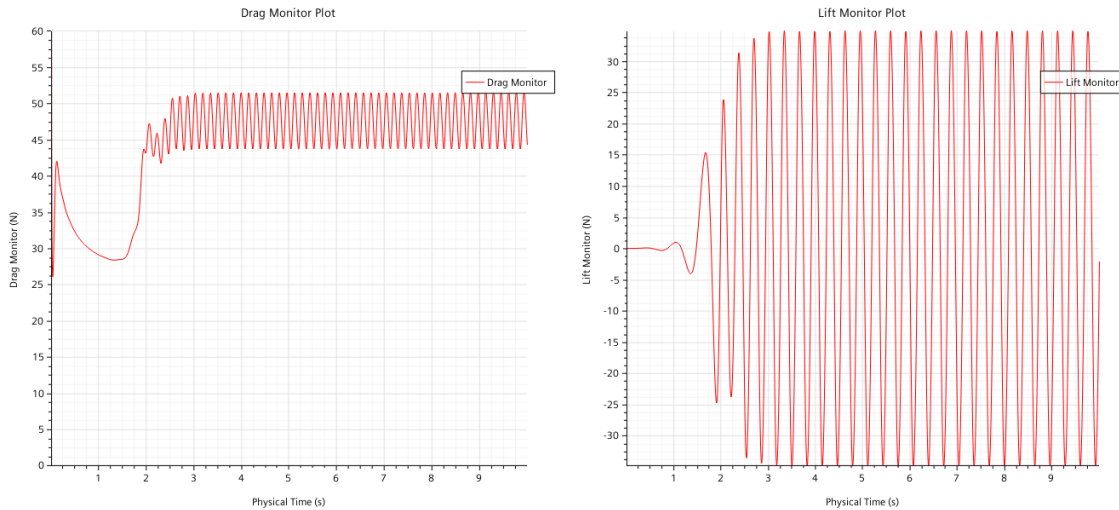
(a) Drag on the Cylinder

(b) Lift on the Cylinder

Figure 6: Force plots used in the verification of the CFD simulation

Vortex shedding frequency f can be predicted by a relation between the Reynolds number Re from Eq. (1) and Strouhal number St from Eq. (5). The results shown here also meet anticipated outcomes based on prior study [9].

IV.2   Verification of Structural Analysis

Star-CCM+'s FEM solver [32] will be compared both to Abaqus's FEM solver [20] and to analytical solutions [16], to ensure it is accurate and suitable for this study. The properties listed in Table 5 are adopted for the verification case.

Table 5: Geometric and material properties selected for the verification tests

Young's Modulus E	100 MPa	Poisson's Ratio ν	0.3
Aspect Ratio	$h_{\text{cyl}} : d_{\text{cyl}} = 10 : 1$	Cylinder Heights	$h_{\text{cyl}} = 10.0$ m

For both simulations and the analytical solution, the load is a traction vector with a 200 N magnitude in the e_x direction, distributed across the entire cylindrical surface.

For the cylinder with the 10:1 aspect ratio, an analytical solution is readily available if the cylinder is treated as a cantilevered beam with a distributed load applied along its entire length. The resulting deflection would be representative of the displacment magnitudes calculated by Star-CCM+ and Abaqus. Table 6 contains the results of this verification case.

Table 6: Structural Verification Case - $h_{\text{cyl}} : d_{\text{cyl}} = 10 : 1$

Solver	Maximum Displacement
Star-CCM+	**5.17 mm**
Abaqus	5.16 mm
Analytical Estimate	5.09 mm

Agreement is strong between Star-CCM+'s FEM solver and Abaqus', and both are close to the analytical estimate using beam equations [16], which becomes more accurate at higher aspect ratios. Thus, we conclude that Star-CCM+ and Abaqus both produced an accurate result. Fig. 7 shows these displacements plotted visually, along with the calculated von Mises stresses.

(a) Displacement (Star-CCM+)

(b) von Mises stress (Star-CCM+)

(c) Displacement (Abaqus)
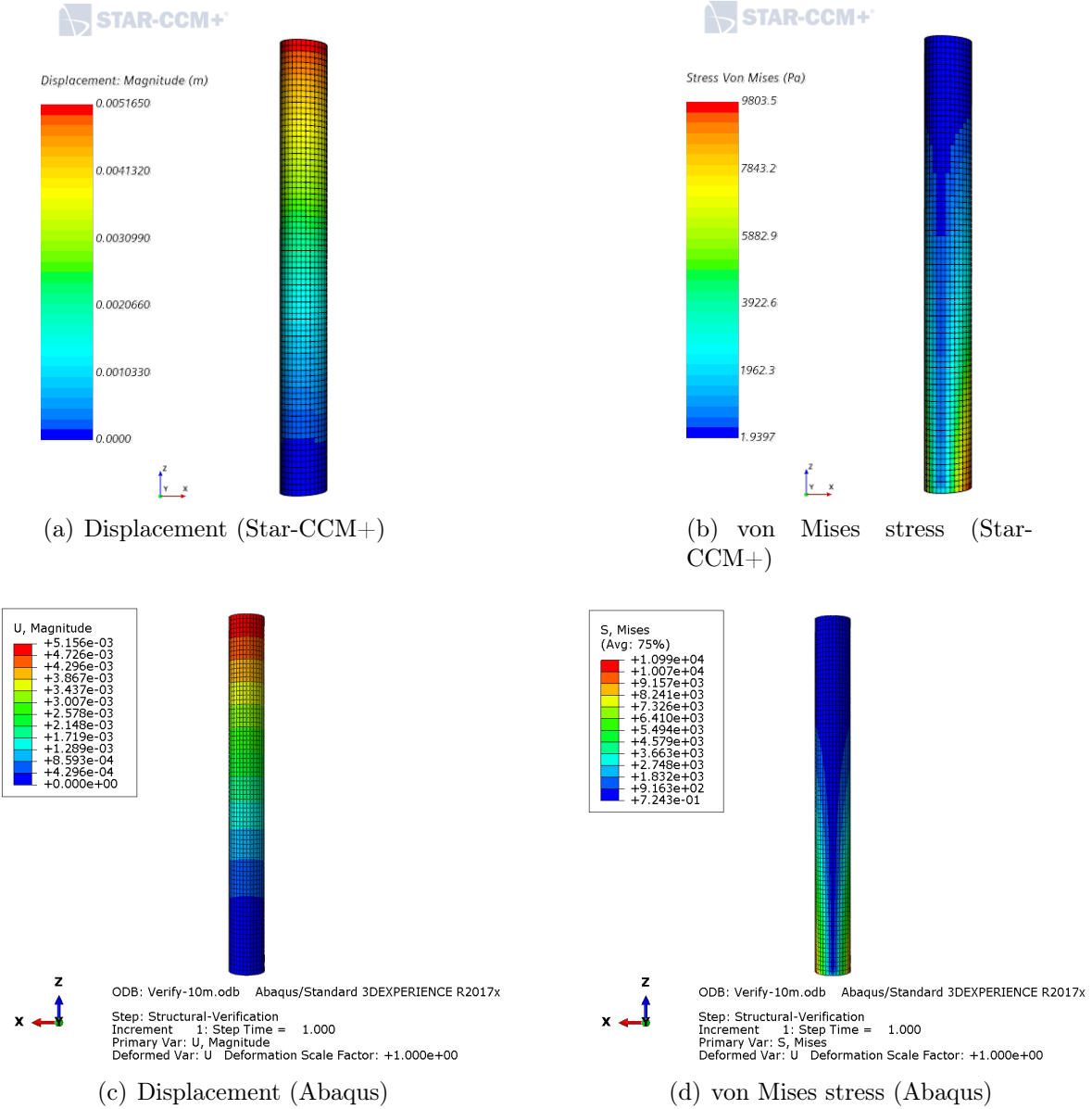

(d) von Mises stress (Abaqus)

Figure 7: Visual displacement and von Mises stress plots for the 10:1 aspect ratio case

With trust in Star-CCM+'s FEM solver, and prior confirmation of the CFD solution's accuracy, we progress to fully-coupled two-way FSI simulations.

IV.3   Mesh Refinement Study

Mesh refinement is carried out here for the fully-coupled, two-way FSI case contained fully within Star-CCM+, with focus on the fluid domain mesh, which proves to be the more computationally intensive of the two domains used in this study.

For all of the meshes used in this study, hexahedral elements are used close to the cylinder, and as a result, the average Δx values presented in the plots are coarser than the level of refinement near the fluid-structure interface.
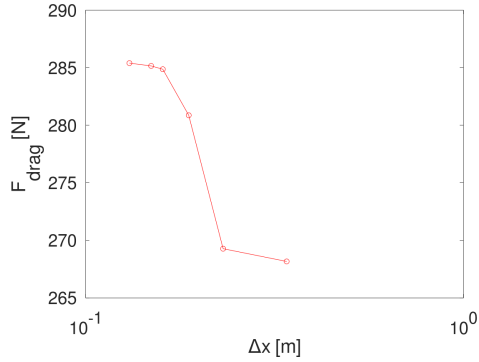
(a) Average drag force on the 1:1 cylinder at different fluid mesh refinement levels
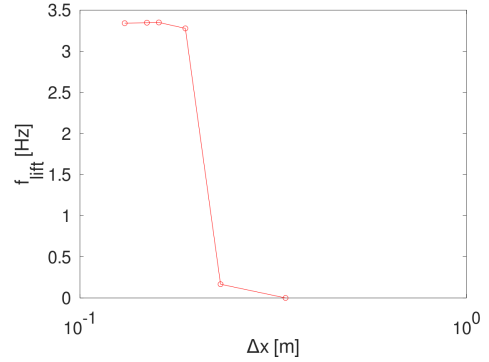
(b) Frequency of the lift force on the 1:1 cylinder at different fluid mesh refinement levels

Figure 8: Comparative Plots of Key Simulation Results used to Evaluate Mesh Suitability and Solution Convergence

The results of this mesh refinement study are seen in Fig. 8, and the ideal balance of efficiency and accuracy appears to be at a refinement level of roughly $\Delta x \approx 0.16$ m.

V   Results & Discussion

Fully-coupled simulations of fluid-structure interaction are carried out as described in the methods, using the meshing parameters decided in the mesh refinement study. Most simulations are carried out for 10 s of simulated time, although some simulations have been cut short as the fluid flow appeared to be fully developed earlier than anticipated, allowing for reductions in computational cost.

V.1   Fluid Loads & Vortex Shedding

As expected from a cylinder in crossflow at low Reynolds numbers, vortex shedding occurs in all simulations as seen, for example, in the streamlines in Fig. 9 and in the time-domain plots of lift and drag forces reported in Fig. 11 and Fig. 13. The clarity of the vortices shed, as well as the amount of high-frequency oscillations in the lift and drag force plots, are impacted both by the cylinder's aspect ratio and its material stiffness.

In most of the simulations, following some initial solution instability, the flow begins to develop fairly quickly, with signs of vortex shedding appearing as early as $t_{\text{solution}} \approx 0.5$ s, with more complete flow development beginning roughly as $t_{\text{solution}} \approx 4.0$ s. The timeframe for flow development, in addition to the exact form this development takes, also depends on the characteristics of the structure. Table 7 lists the frequencies with greatest amplitude present in each of the tested cases.

Table 7: Frequencies of greatest amplitude in each of the lift plots obtained in the isotropic test cases.

	$h_{\text{cyl}} = 0.5$ m	$h_{\text{cyl}} = 1.0$ m	$h_{\text{cyl}} = 5.0$ m
$E = 100$ GPa	0.3000 Hz	1.700 Hz	1.300 Hz
$E = 100$ MPa	0.5000 Hz	1.700 Hz	-
$E = 100$ kPa	0.3636 Hz	-	155.2 Hz

Simulation:
- Isotropic "Near-Rigid" 1.0 m Cylinder

Details:
- Slice taken at $z = 0.5$ m
- Solution Time: 4.0 s $\leq t \leq 5.0$ s
- Vortices frequently lose definition later in the wake due to coarsening of the fluid domain mesh.
- Vortex shedding begins in this simulation around $t = 2$ s, but becomes more developed around $t = 4$ s.
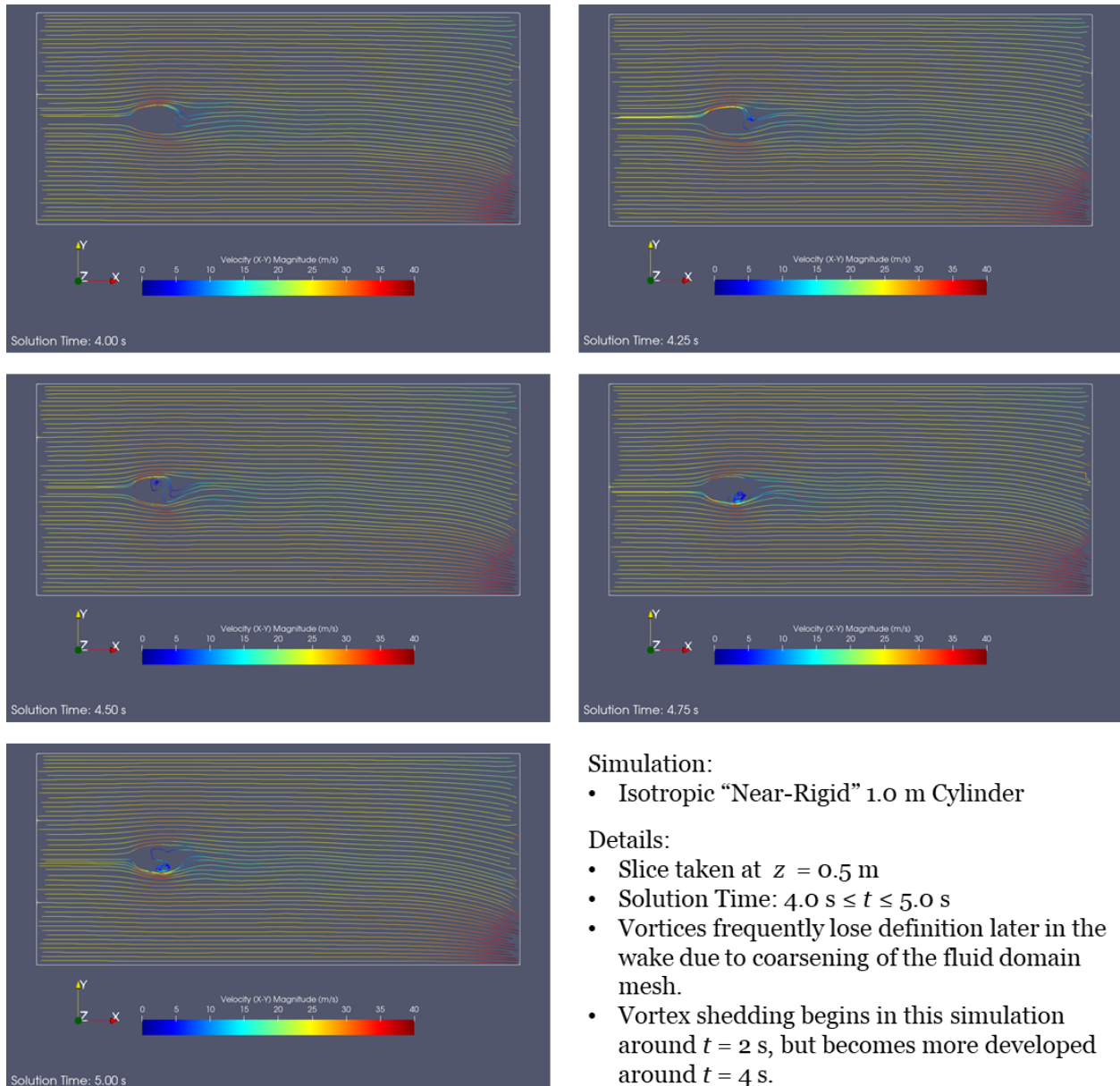
Figure 9: Streamlines illustrating the characteristic vortex shedding behavior exhibited by cylinders under crossflow at low Reynolds numbers

V.1.1 Impacts of Cylinder Stiffness on Fluid Loads & Vortex Shedding

Visualizing the wake as it develops, little difference appears between the three selected structural stiffnesses, as seen in Fig. 10. This suggests that, at least for isotropic materials, the initial phase of flow development is largely independent of structural stiffness.

However, upon closer inspection of the lift imparted on the cylinders, the effects of material stiffness are much more readily apparent, as seen in Fig. 11. Fewer separate frequencies appear in the lift plot for the most rigid cylinder, while the mid-range cylinder has some higher frequencies appearing, that would not be explained by vortex shedding alone. Likewise, the softest cylinder has far more frequencies appearing. This suggests that softening of material causes changes in frequency, as well as creating more high frequency activity in the lift.

The softest case in Fig. 11 is of particular interest, as it exhibits frequencies far higher than the other 0.5 m cases, particularly in the 30 Hz $\leq f_{\text{lift}} \leq$ 70 Hz range. This suggests that in this softest case, the material deformation has a significant impact on the dynamic characteristics of this cylinder. For the 'mid-range' and 'near-rigid' cases, no notable frequencies appear beyond $f_{\text{lift}} = 10$ Hz.

Each of these cases exhibits a 'primary' frequency in the 0.5 Hz $\leq f_{\text{lift}} \leq$ 1 Hz range, and while this is in the same order of magnitude as the vortex shedding frequency one would predict via empirical relations between the Reynolds number Re and Strouhal number St, the dominant frequencies in the simulation are lower than the empirical prediction would suggest. This could be attributed to the deformation of the cylinder, as relations between Re and St in the literature assume the cylinder is rigid and stationary, and when the cylinder deforms, the Strouhal number St will likely depend on the deformation of the cylinder to some extent, rather than just on the Reynolds number Re as seen in Eq. (5). The reason one might expect a deformable cylinder to reduce the frequency of vortex shedding could be
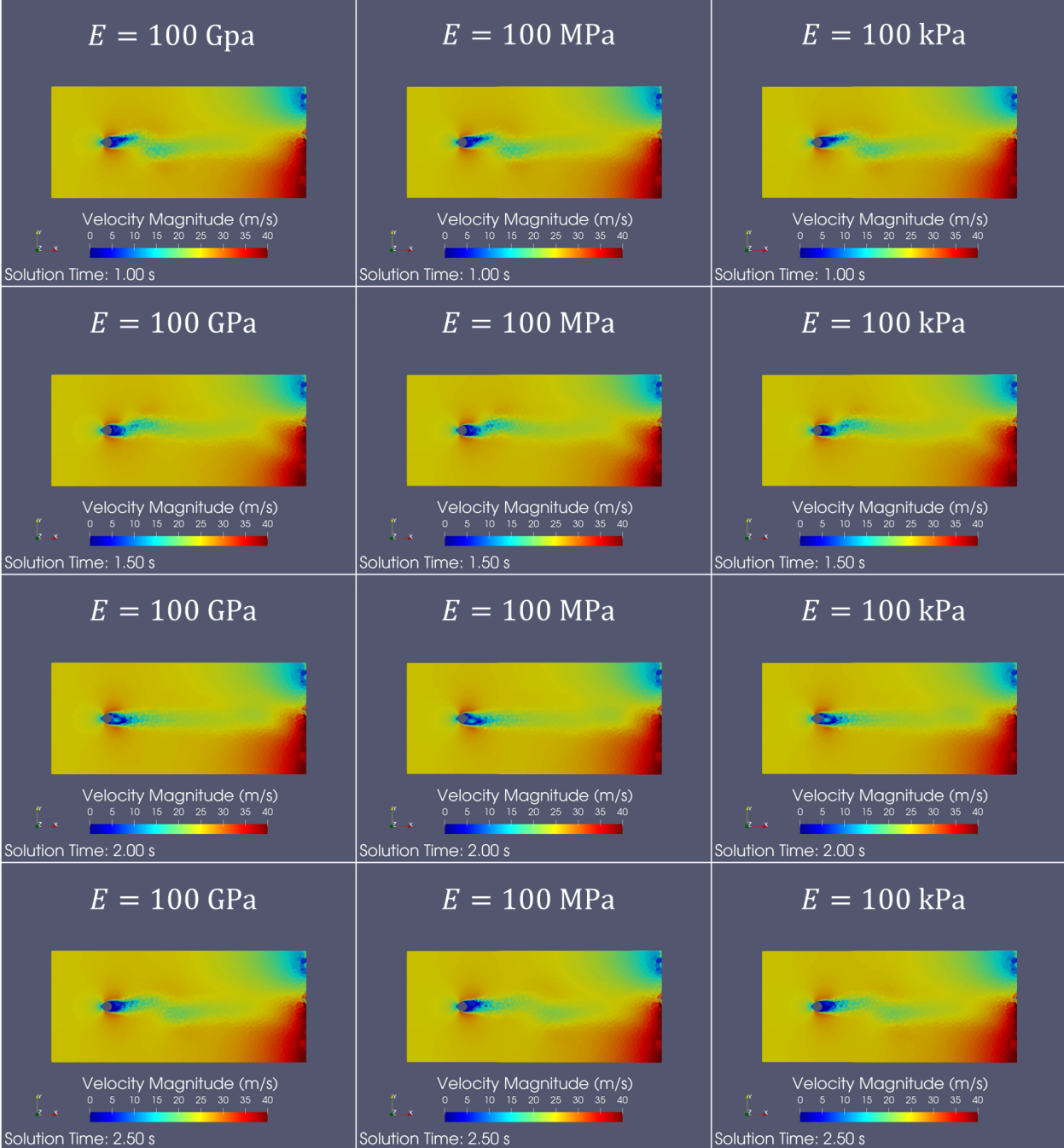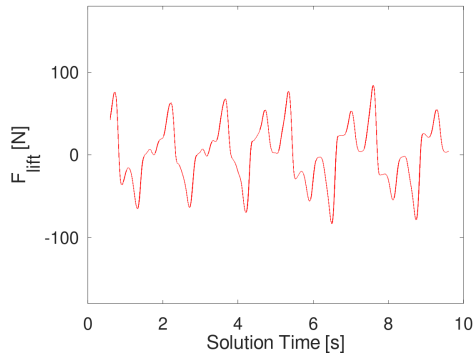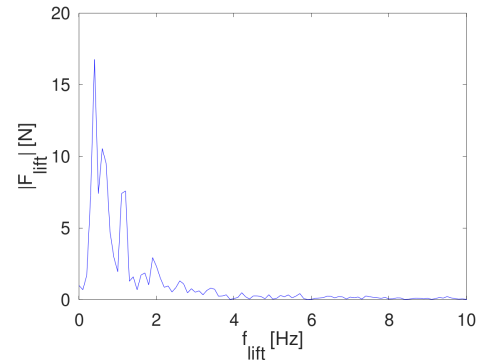
Figure 10: Wake comparison between the selected isotropic stiffness levels for the cylinder with $h_{\mathrm{cyl}} = 0.5$ m
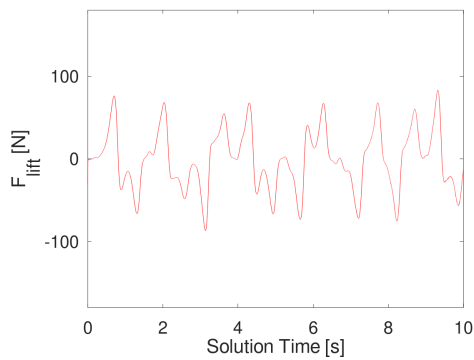
due to the cylinder's ability to absorb energy as strain energy.

(a) Time-domain plot of lift forces when $E = 100$ GPa

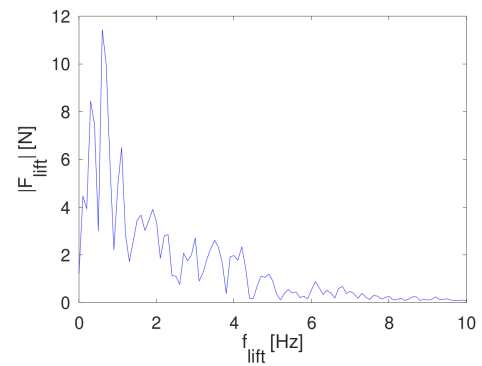(b) Frequency-domain plot of lift forces when $E = 100$ GPa

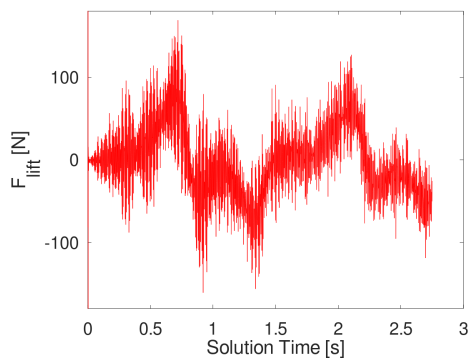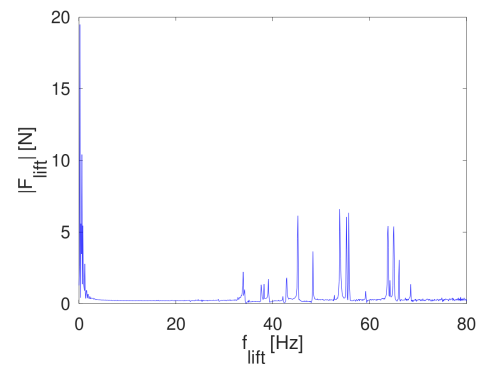(c) Time-domain plot of lift forces when $E = 100$ MPa

(d) Frequency-domain plot of lift forces when $E = 100$ MPa

(e) Time-domain plot of lift forces when $E = 100$ kPa

(f) Frequency-domain plot of lift forces when $E = 100$ kPa

Figure 11: Comparison of lift forces on the 0.5 m cylinders with differing Young's moduli in the time and frequency domains

Application of the softest material to the case where $h_{cyl} = 5.0$ m results in significant amounts of bending relative to the 'near-rigid' case for the same cylinder height. Fig. 12 displays a few noteworthy features, and while the variability in behavior with respect to height along the cylinder is to be expected (and will be explored further shortly), the bending behavior has created notable vertical movement in the flow, particularly immediately behind the cylinder. Additionally, the sharp edge of the cylinder's top circular surface also introduces some separation in the wake that, in its upper portion, is primarily fed by flow leaving the top circular surface of the cylinder. The lower portion of the wake behind the cylinder is instead primarily due to the flow traveling about the cylinder's vertical sides.

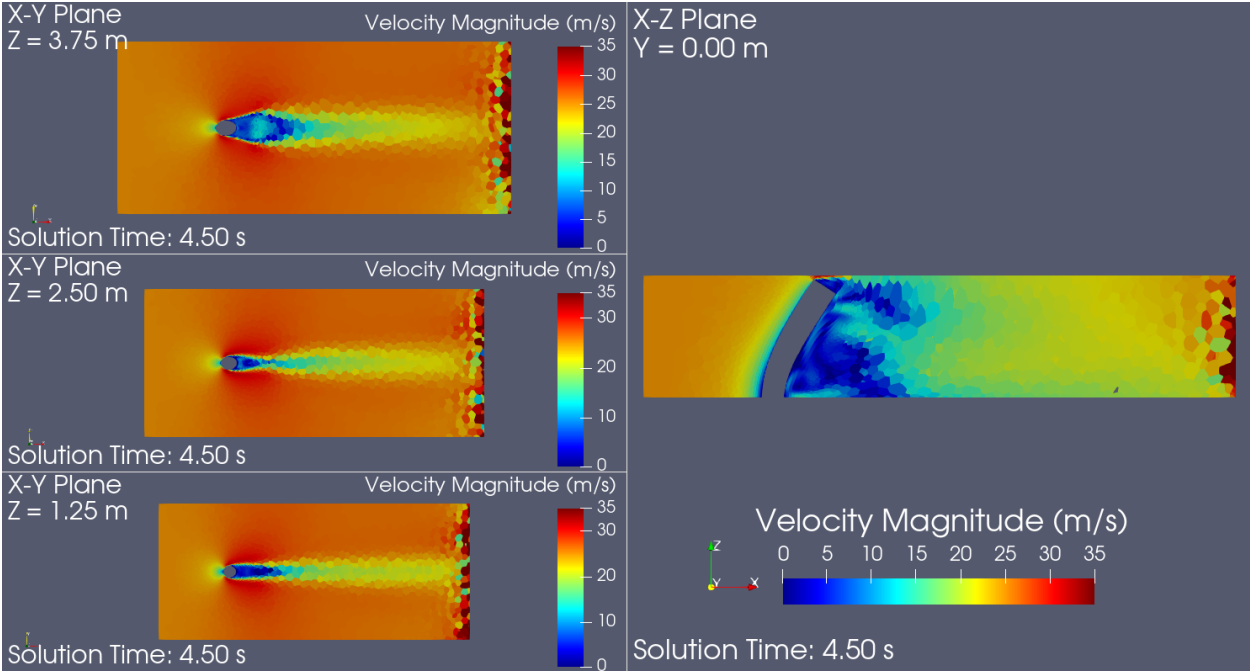

Figure 12: Fluid flow in the wake of the cylinder when $h_{cyl} = 5.0$ m and $E = 100$ kPa

V.1.2 Impacts of Cylinder Aspect Ratio on Fluid Loads & Vortex Shedding

Of the cases tested, typically, the cylinders with $h_{cyl} = 1.0$ m resulted in the least noisy and most stable simulations. For the cylinders with $h_{cyl} = 0.5$ m, the fluid's shearing behavior

on the top circular face of the cylinder is a significant factor in the simulated outcome, and leads to a high frequency content in the lift forces (Fig. 13). This high frequency content is particularly visible in the frequency plot, where despite multiple peaks appearing at the lower frequencies expected to be created by the vortex shedding, high frequency peaks are present up to the 50-Hz range. The cylinders with $h_{cyl} = 5.0$ m tend to exhibit even more high-frequency behavior in their results, however, with frequencies appearing as high as $f_{lift} = 250$ Hz. Additionally, as seen in Fig. 13, the lift frequencies lack a single well-defined peak for the $h_{cyl} = 5.0$ m case, instead displaying both low-frequency and high-frequency peaks.

One potential explanation for the behavior of the 5.0 m case is a more complex 3-dimensional vortex structure, where different vortices form at different heights along the cylinder. Considering the streamlines on the 5.0 m case, shown in Fig. 14, this is likely a contributor to the significant high-frequency activity present in this case, due to the different directions in which the vortices shed at different heights on the cylinder.

As expected, the average drag is significantly higher for the cylinders with greater heights, as seen in Table 8, due primarily to the increased surface area that results from increasing h_{cyl}. The relation between drag force F_{Drag} and cylinder height h_{cyl} is roughly linear, as one would expect, as drag force relates linearly to the wetted surface area of the structure, which itself relates linearly to cylinder height.

Table 8: Average Drag for Cylinders of Varying Aspect Ratios with $E = 100$ GPa

Simulation Case	Average Drag (from $t_{solution} \geq 5.000$ s)
$h_{cyl} = 0.5$ m	142.022 N
$h_{cyl} = 1.0$ m	286.731 N
$h_{cyl} = 5.0$ m	1510.841 N
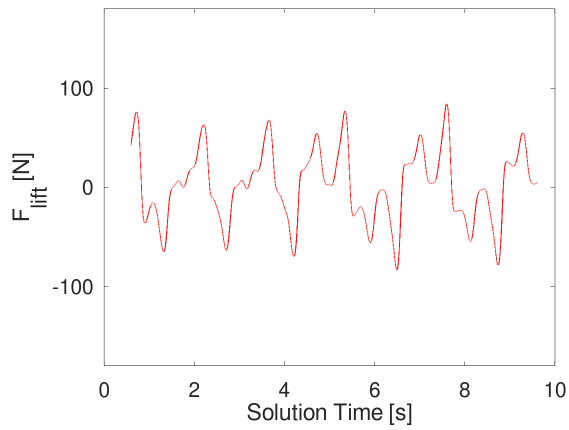
(a) Lift in the time domain for the 1:2 cylinder
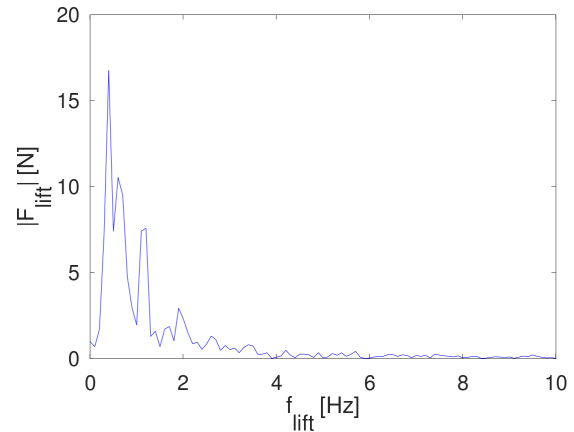
(b) Lift in the frequency domain for the 1:2 cylinder
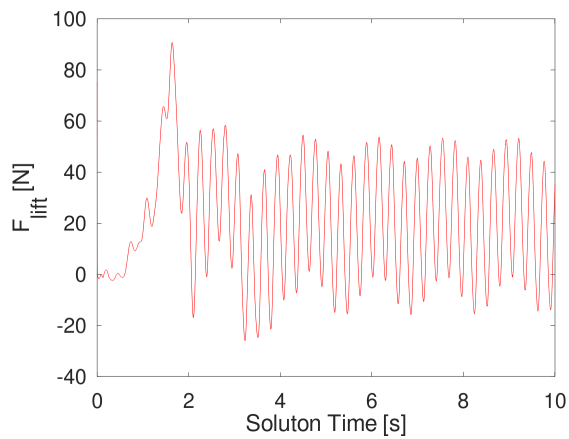
(c) Lift in the time domain for the 1:1 cylinder
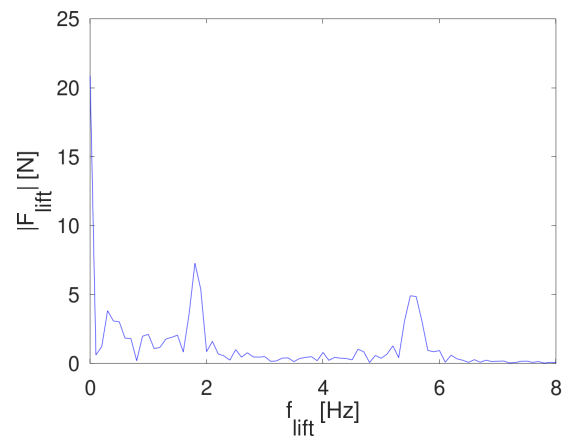
(d) Lift in the frequency domain for the 1:1 cylinder
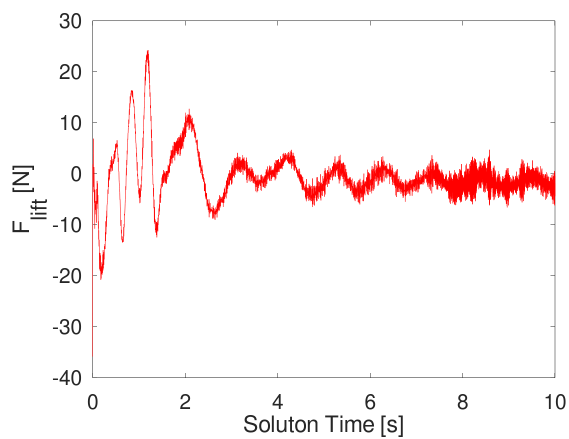
(e) Lift in the time domain for the 5:1 cylinder
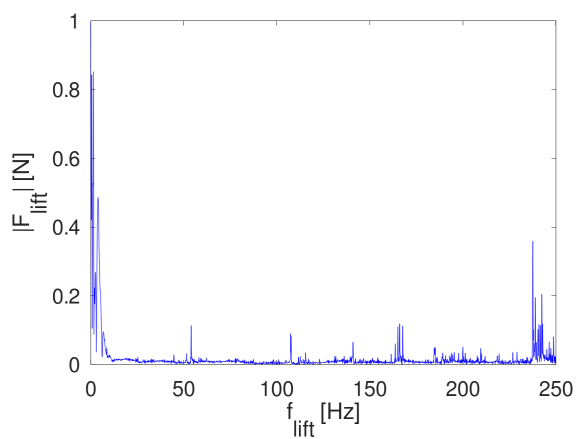
(f) Lift in the frequency domain for the 5:1 cylinder

Figure 13: Comparison of lift forces F_{lift} and frequencies f_{lift} for cylinders of differing aspect ratios. In all cases here, $E = 100$ GPa.

Figure 14: Vortex shedding in different directions at different heights on the cylinder with $h_{\mathrm{cyl}} = 5.0$ m and $E = 100$ GPa
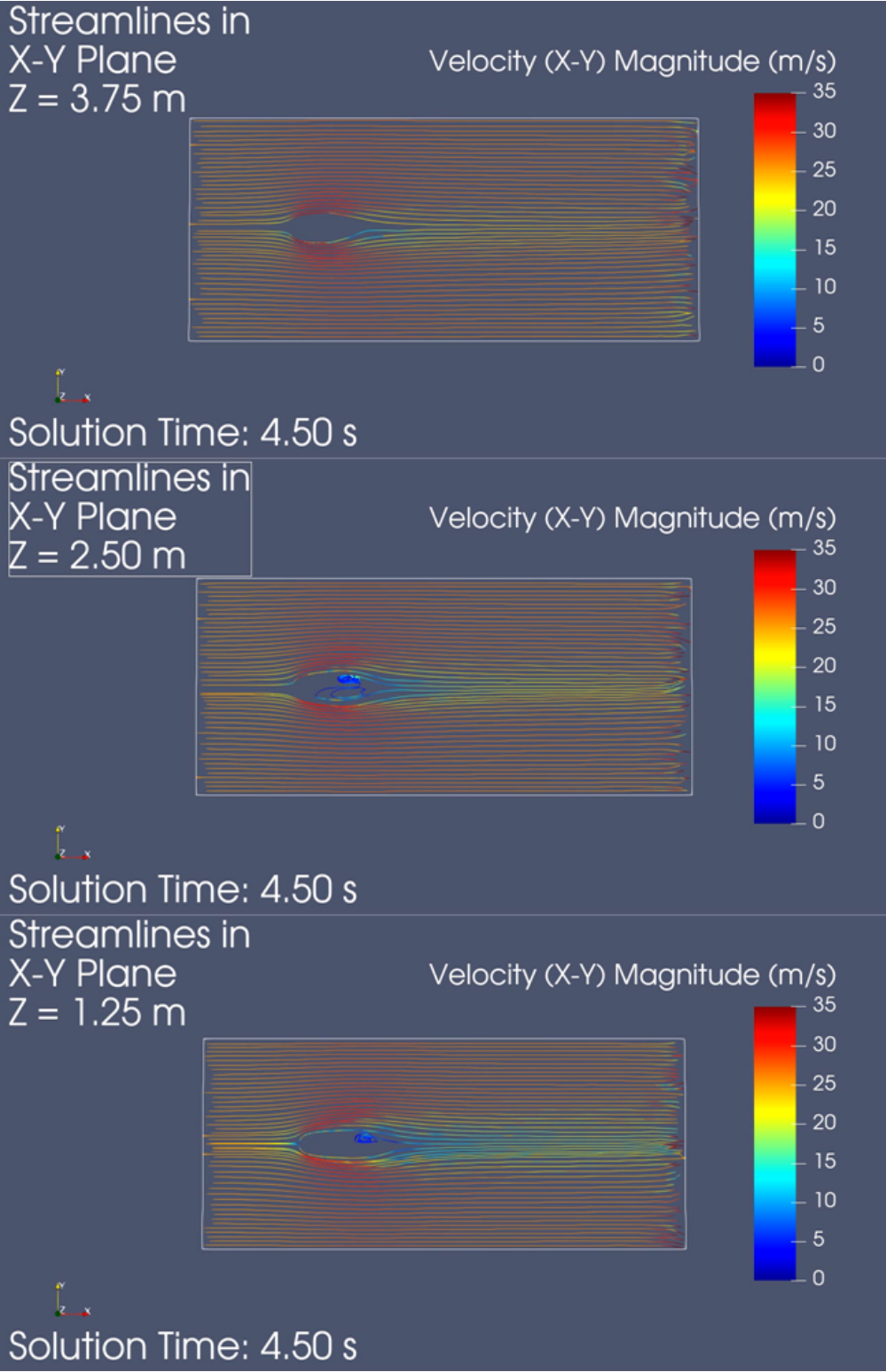
V.2 Structural Deformation & Stresses

V.2.1 Impacts of Cylinder Stiffness on Structural Deformation & Stresses

Fig. 15 highlights the impact of the stiffness, in terms of Young's Modulus E, on the deformation and general behavior of the cylinder from a structural standpoint.

One noteworthy behavior highlighted in Fig. 15 is the 'cratering' and subsequent 'bubbling' behavior that occurs on the circular surface at the top of the cylinder. As the 'cratering' occurs, the cylinder also experiences localized increases in diameter roughly halfway down the cylindrical face. During the 'bubbling' phase, the diameter instead decreases halfway down the cylinder. The case with $E = 100$ kPa is particularly interesting in its behavior, as some of the 'cratering' and 'bubbling' motions interfere with one another, and the cylinder sometimes develops a crater with raised edges, or a bubble with its edge sunken beyond the original height of the circular surface. Additionally, in the cylindrical surface for the $E = 100$ kPa case as well, certain areas of the cylinder seem to increase and decrease in their distance from the cylinder's center independently of one another, a behavior not exhibited by the other two isotropic cases. Further refinement of the solid mesh is required to better investigate this behavior.
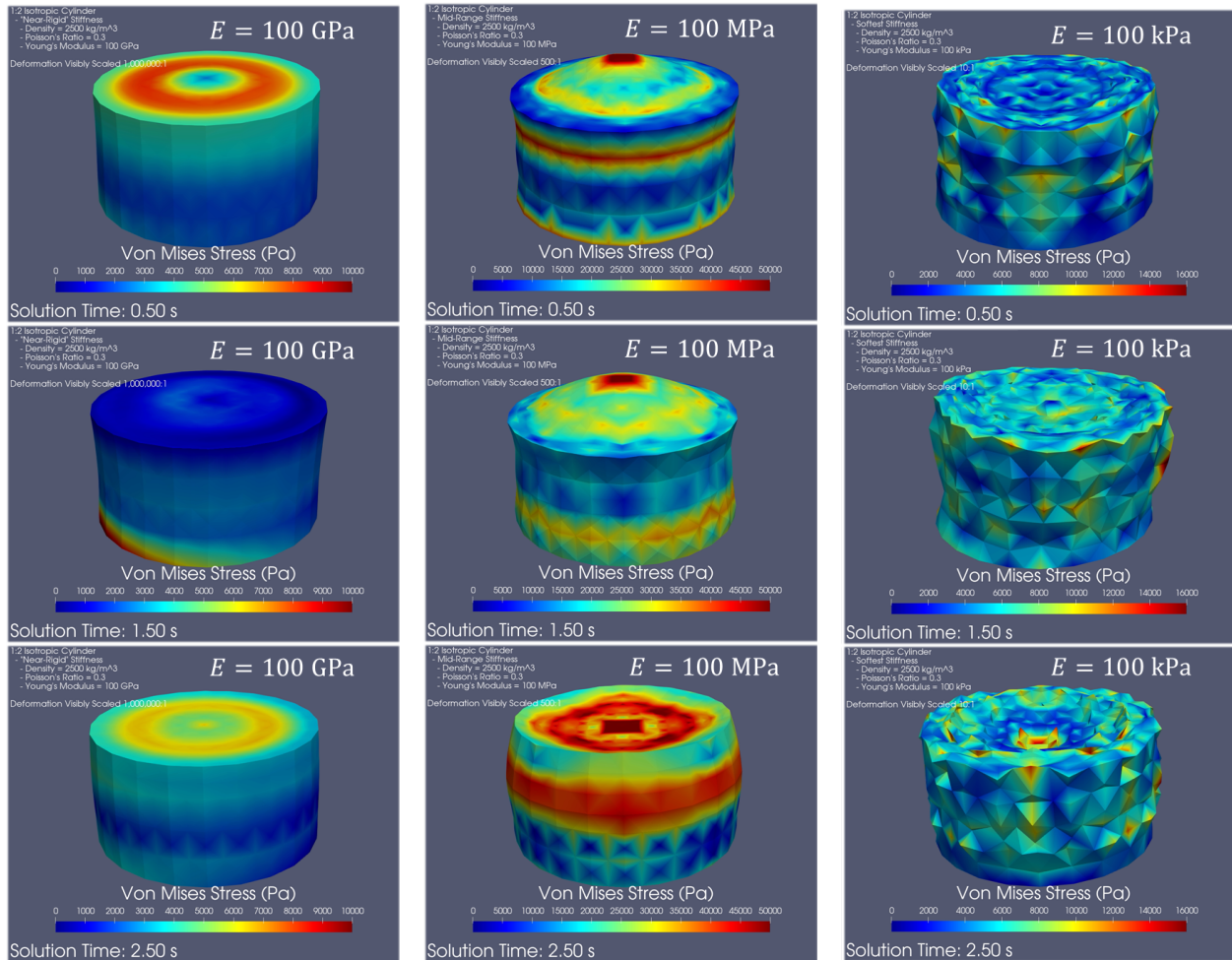
(a) Deformation of the 0.5 m cylinder when $E = 100$ GPa. Deformation is scaled at 100,000:1.

(b) Deformation of the 0.5 m cylinder when $E = 100$ MPa. Deformation is scaled at 500:1.

(c) Deformation of the 0.5 m cylinder when $E = 100$ kPa. Deformation is scaled at 5:1.

Figure 15: Visual comparison of deforming cylinders with $h_{\mathrm{cyl}} = 0.5$ m and decreasing Young modulus (left to right), colored according to localized von Mises stresses.

V.2.2 Impacts of Cylinder Aspect Ratio on Structural Deformation & Stresses

The introduction of different cylinder heights has predictable effects with respect to cylinder deformation behavior: greater aspect ratios lead to increased bending (Fig. 16). As expected, the cases experiencing higher bending also see higher von Mises stresses at their fixed bases, particularly in the regions most directly facing the inlet or outlet of the fluid domain.

33
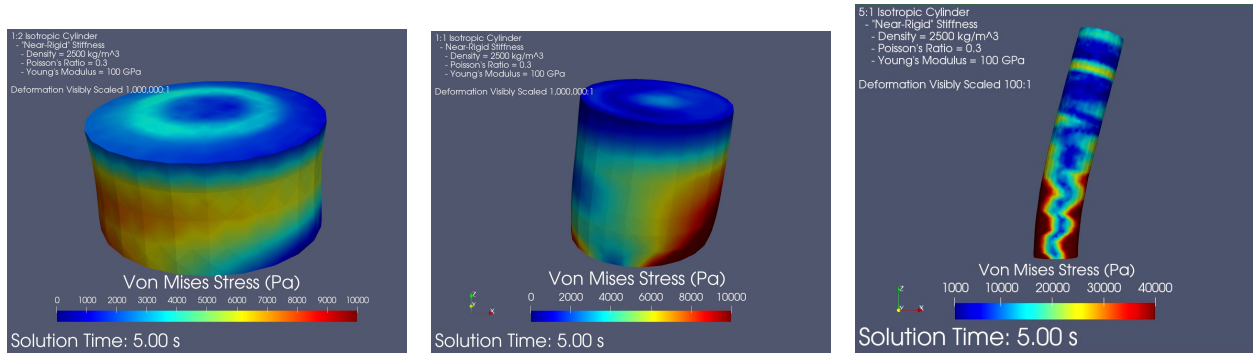
(a) Isotropic 1:2 cylinder, with minimal deformation. Deformation is scaled at 1,000,000:1.

(b) Isotopic 1:1 cylinder, with some deformation. Deformation is scaled at 1,000,000:1.

(c) Isotopic 5:1 cylinder with substantial defomation. Defomation is scaled at 100:1

Figure 16: Comparison of deformed isotropic cylinders of differing aspect ratios at $t_{\text{solution}} = 5.00$ s, colored by von Mises stress. $E = 100$ GPa.

V.2.3 Dynamic Characteristics of the 5:1 Cylinder

As seen in Figs. 17 and 18, the most rigid of the 5.0 m cases exhibits a deflection reversal behavior not seen in other simulations: when the cylinder bends under fluid loads and reaches its maximum deflection, it rebounds. This occurs with a frequency of roughly 1.1 Hz and an amplitude of roughly 3.5 mm.
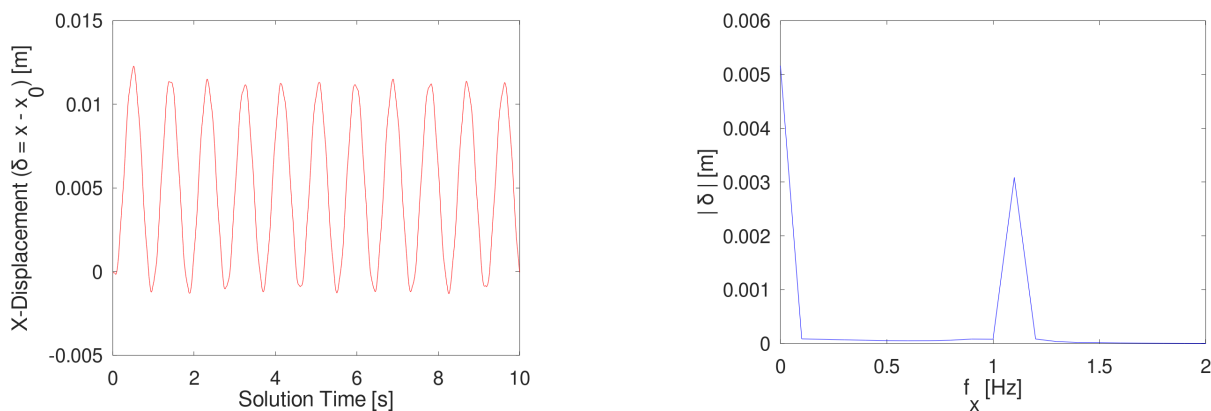
(a) Displacement of the cylinder's center point on the top face in the time domain

(b) Displacement of the cylinder's center point on the top face in the frequency domain

Figure 17: Displacement plots of the 5:1 cylinder's top-face center when $E = 100$ GPa

34
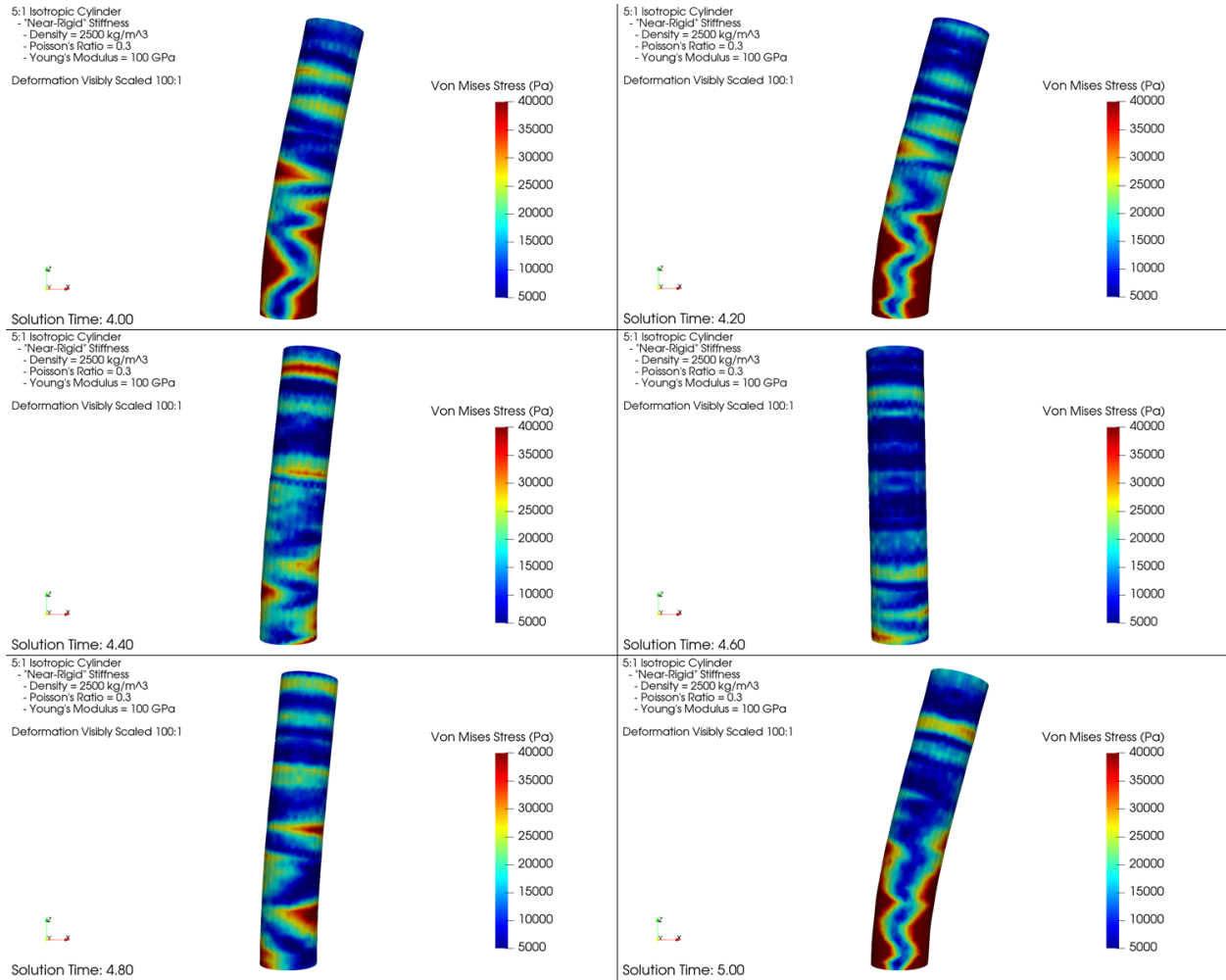
Figure 18: Deformation and recovery behavior through time of the 5:1 cylinder with $E = 100$ GPa, scaled at 100:1 and colored by von Mises stresses

Fig. 17 shows the displacement component parallel to the freestream fluid flow for the center point on the top circular face. The case with $E = 100$ GPa also exhibits zig-zag patterns in its von Mises stresses in the bottom half of the cylinder, as seen in Fig. 18. This case also oscillates with the Y-axis as well, but the oscillations are far smaller than those along the X-axis.

While the case with $E = 100$ GPa has its unique rebound behavior, such behavior is absent in the case with $E = 100$ kPa, which rather than rebounding, continues to deform further under the fluid loads as seen in Fig. 19. However, in this case the upper portion of
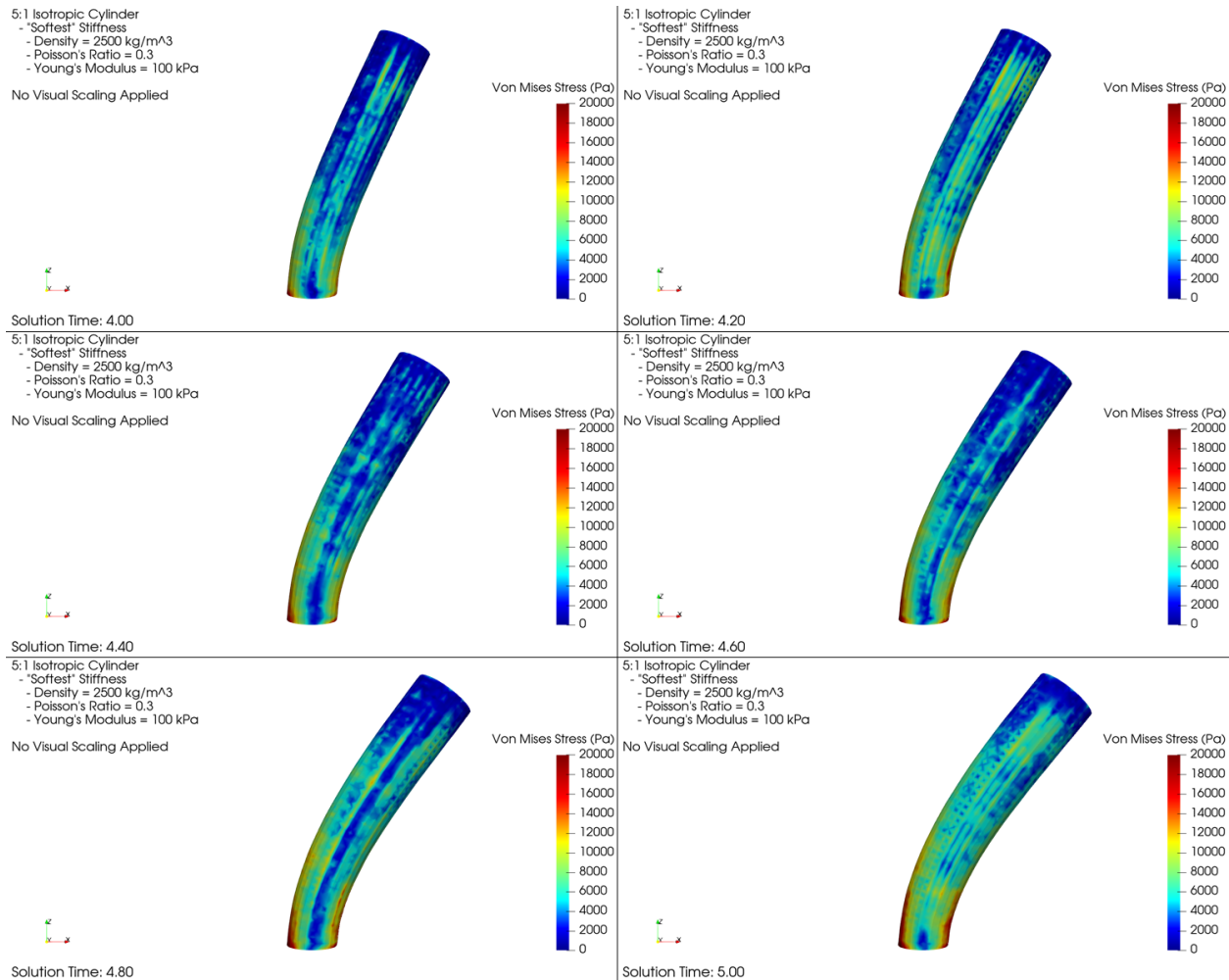
Figure 19: Deformation behavior through time of the 5:1 cylinder with $E = 100$ kPa, colored by von Mises stresses

the cylinder grows wider as the cylinder is bent further. Like the 100 GPa case, this case also exhibits small oscillations along the Y-axis.

V.3   Effects of Anisotropic Elastic Properties on Fluid-Structure Interaction

The introduction of anisotropic material properties causes the cylinder to deform differently in different directions, as expected based on the anisotropy of the material strength. The

36

directionally-dependent deformation also creates some asymmetry in the fluid wake.

When comparing the 0.5 m anisotropic case to a baseline isotropic case where $E = 100$ GPa, the lift plots seen in Fig. 20 appear. As one might expect from the earlier isotropic work, the introduction of the anisotropy results in high frequency content in the lift plot, as the anisotropic material is softer than 100 GPa. However, the anisotropic material's application results in a plot with more high-frequency activity than the case with $E = 100$ MPa in Fig. 11, w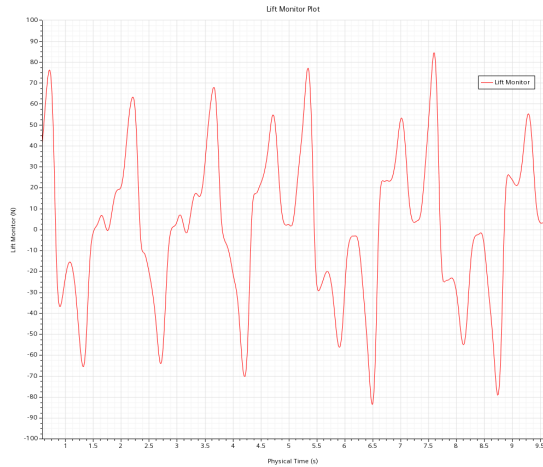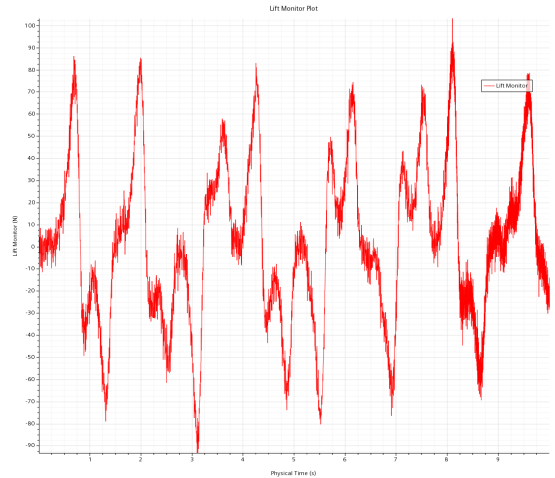hich may be due to the anisotropic material's matrix being far softer. The result of the softer matrix is that the cylinder more readily deforms in some directions than others, where the stiffest direction is aligned with the fibers.

(a) Lift on the isotropic cylinder with $h_{\mathrm{cyl}} = 0.5$ m and $E = 100$ GPa

(b) Lift on the cylinder with $h_{\mathrm{cyl}} = 0.5$ m and anisotropic material properties

Figure 20: Time-domain lift comparison between the isotropic and anisotropic 0.5 m cylinders.

As seen in Fig. 21, while the lift in the isotropic case began with large amplitudes and damped itself down to lower amplitudes with higher frequencies, the anisotropic case begins with very small amplitudes before rapidly growing, with significant high-frequency activity and no easily visible 'main' frequency in the lower-frequency range.

While the anisotropic cases both introduce more high-frequency activity to the lift plots, the impacts on their frequencies differs between the 1:2 and 5:1 cases. Fig. 22 displays the

(a) Lift on the isotropic cylinder with $h_{\mathrm{cyl}} = 5.0$ m and $E = 100$ GPa
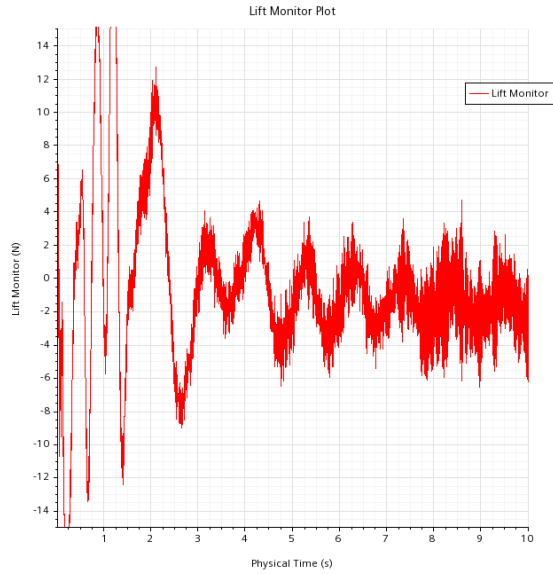
(b) Lift on the cylinder with $h_{\mathrm{cyl}} = 5.0$ m and anisotropic material properties
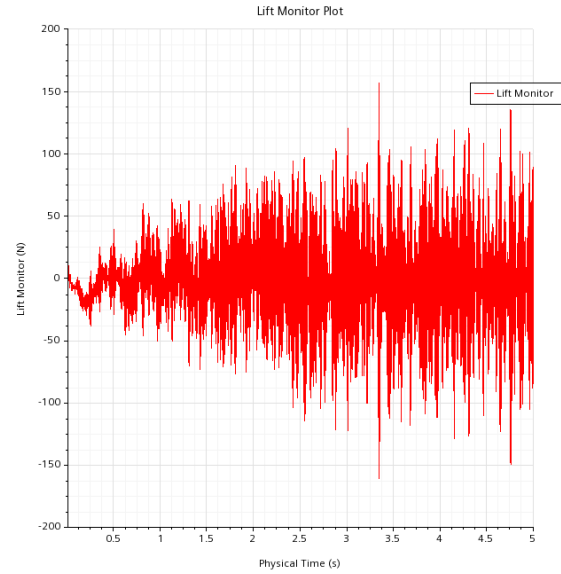
Figure 21: Time-domain lift comparison between the isotropic and anisotropic $5.0\,\mathrm{m}$ cylinders.

frequencies present in the lift plots for each of the anisotropic cases. The anisotropic 1:2 case lacks many higher frequencies, and only displays a bit more low-frequency activity than the isotropic 1:2 cases seen in Fig. 11. However, the 5:1 case displays significant higher-frequency activity in the 400 Hz to 500 Hz range (Fig. 21).

From a structural standpoint, in the 1:2 cylinder, the 'cratering' and 'bubbling' phenomena previously seen in Fig. 15 are still present, but rather than being almost radially symmetric about the center, the 'craters' and 'bubbles' show symmetry about the Y-axis as seen in Fig. 23. This can be attributed to the orientation of the preferential axis in the anisotropic material, which was in the Y-Z plane. This occurs even though the flow direction is perpendicular to the Y-axis, meaning this near-symmetry exists perpendicularly to the flow direction as well. This indicates that the preferential axis' orientation likely plays a significant role in the determination of structural behaviors for cylinders with anisotropic elasticity undergoing crossflow with low Reynolds numbers.
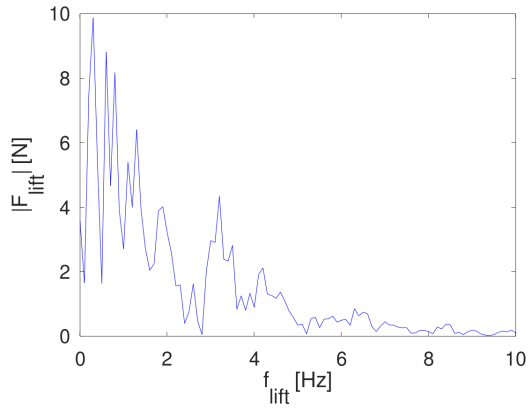
(a) Frequencies present in the lift plot for the anisotropic 1:2 case
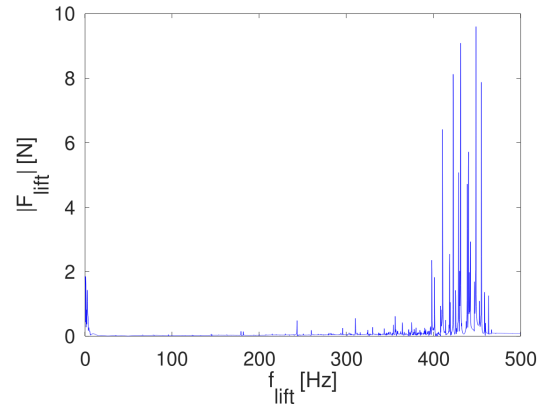
(b) Frequencies present in the lift plot for the anisotropic 5:1 case

Figure 22: Comparison between frequency-domain plots of lift for the 1:2 and 5:1 anisotropic cylinders
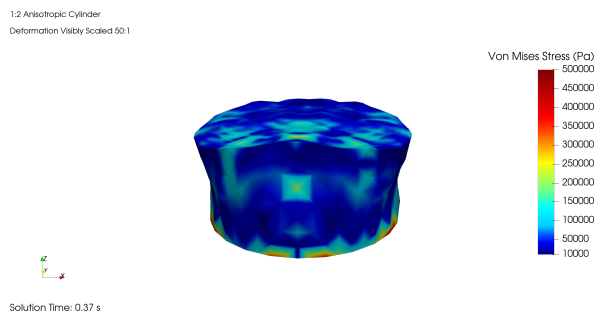
(a) The anisotropic 1:2 cylinder at $t_{\text{solution}} = 0.37$ s, featuring a 'bubble' with symmetry about the Y-axis
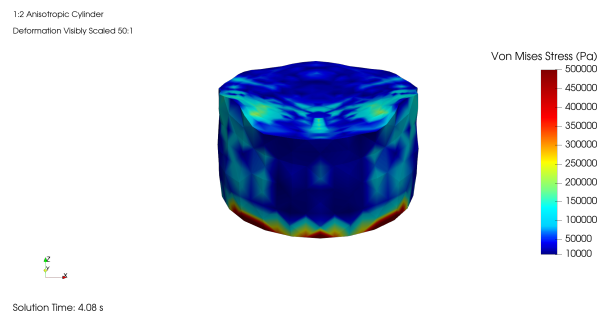
(b) The anisotropic 1:2 cylinder at $t_{\text{solution}} = 4.08$ s, featuring a 'crater' with symmetry about the Y-axis

Figure 23: Deformation on the anisotropic 1:2 cylinder exhibiting symmetry about the Y-axis

The anisotropic 1:2 cylinders also exhibit a 'flowering' phenomenon visible on the cylinder's cross-section. The cylinder frequently forms shapes like those shown in Fig. 24, and often the circular shape of the cross-section more closely resembles non-circular polygons, but with rounded corners. The 'flowering' behavior also exhibits near-symmetry about the Y-axis.
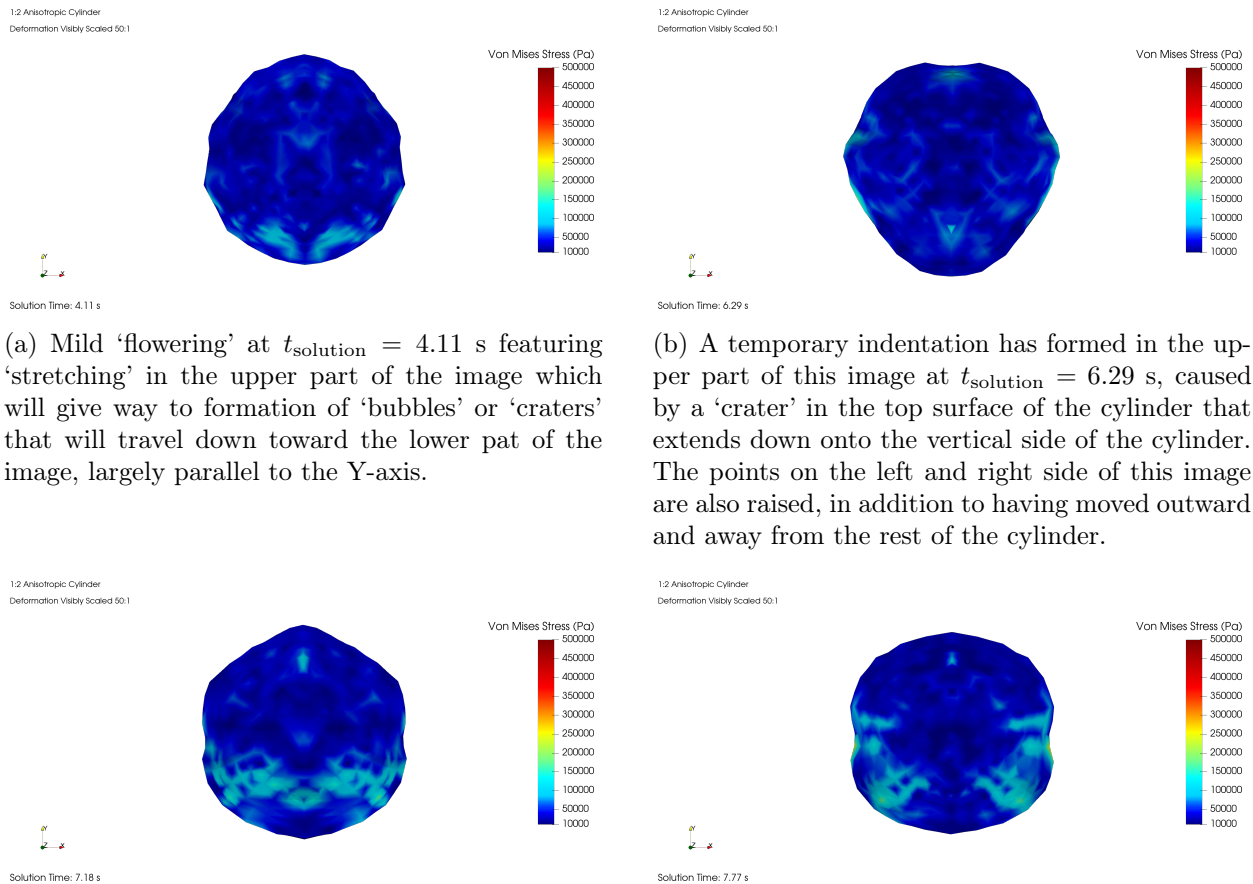
(a) Mild 'flowering' at $t_{\text{solution}} = 4.11$ s featuring 'stretching' in the upper part of the image which will give way to formation of 'bubbles' or 'craters' that will travel down toward the lower pat of the image, largely parallel to the Y-axis.

(b) A temporary indentation has formed in the upper part of this image at $t_{\text{solution}} = 6.29$ s, caused by a 'crater' in the top surface of the cylinder that extends down onto the vertical side of the cylinder. The points on the left and right side of this image are also raised, in addition to having moved outward and away from the rest of the cylinder.

(c) At $t_{\text{solution}} = 7.18$ s, the cylinder has developed concave areas on its sides in both the leading and trailing faces, despite the loading conditions being different between those areas.

(d) At $t_{\text{solution}} = 7.77$ s, the concave regions have formed again, but the top and bottom sides of this image are much more rounded and closer to symmetrical than in the previous images.

Figure 24: Varying examples of the anisotropic 1:2 cylinder's 'flowering' behavior in different stages, viewed from the top surface with coloring corresponding to the von Mises stress

The anisotropic 5:1 cylinder lacks the 'flowering' phenomenon, but like the isotropic 5:1 case with $E = 100$ GPa, the anisotropic cylinder oscillates slightly along both the X- and

Y-axes, as can be seen without visible scaling applied in Fig. 27, and in the displacement plots provided in Fig. 25 and Fig. 26.
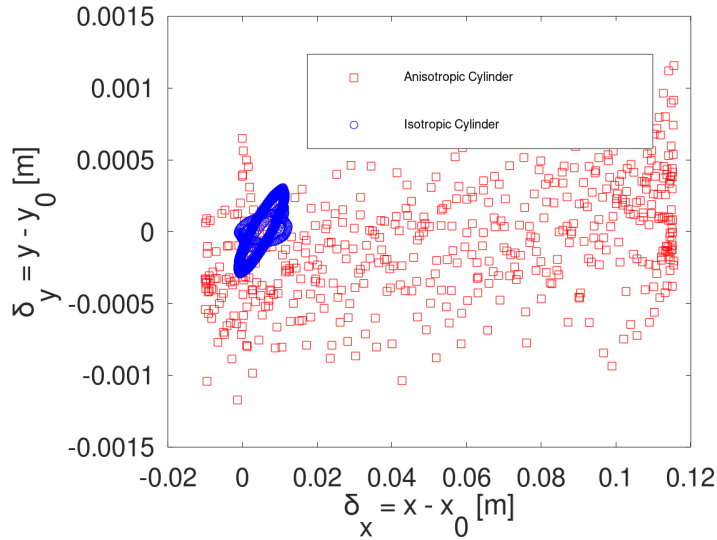
Figure 25: Isotropic and anisotropic 5:1 cylinders' centerpoints on their top faces, traced in the x-y plane

As anticipated, the anisotropic 5:1 cylinder deforms more readily than its stiffer counterpart, as evidenced by the much larger displacements traced in Fig. 25. However, due to a phase shift between the X- and Y-displacements δ_x and δ_y, the correlation between the two displacements is weaker for the anisotropic case than the isotropic case. This is suspected to be a result of the anisotropic material, as the preferential axis results in additional resistance to δ_y over δ_x.
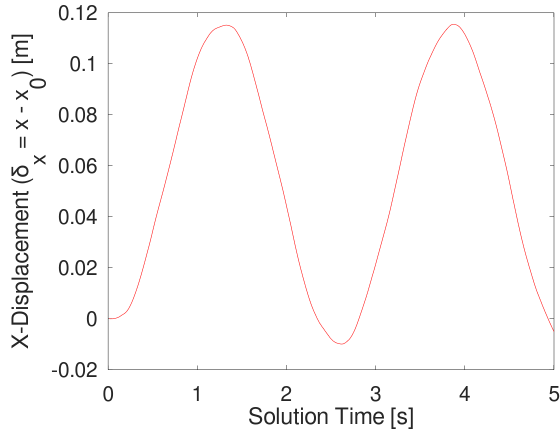
(a) Time-domain plot of δ_x
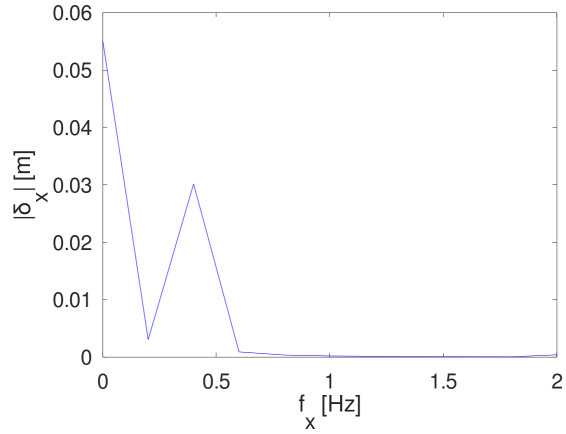
(b) Frequency-domain plot of δ_x
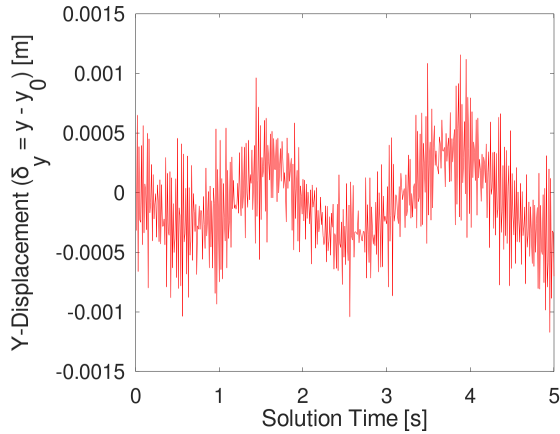
(c) Time-domain plot of δ_y
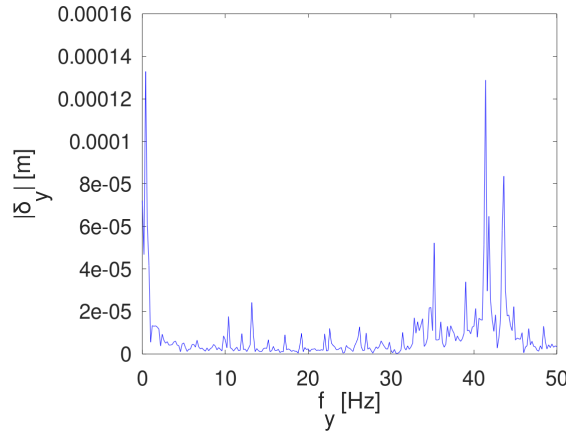
(d) Frequency-domain plot of δ_y

Figure 26: Time- and frequency-domain plots of δ_x and δ_y for the anisotropic 5:1 cylinder

Per Fig. 26, the amplitude of δ_x is much greater than that of δ_y, due to the greater resistance to δ_y afforded by the anisotropic elasticity and because the majority of the load induced by the fluid flow is parallel with the flow's direction and δ_x. However, while δ_x lacks any activity at frequencies above 1 Hz, δ_y has significant higher-frequency activity, and the peak near 41 Hz in Fig. 26 is almost as significant in amplitude as the far lower frequency activity near to 1 Hz.

Stress Von Mises (Pa)
0   25000   50000
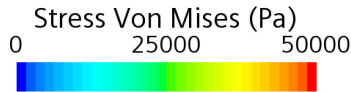
Solution Time 1 (s)

(a) At $t_{\mathrm{solution}} = 1$ s, the stress in the cross-section displays a pair of perpendicular lines: a high-stress line aligned with the preferential axis of the material, and a lower-stress line perpendicular to the preferential axis. The high-stress line also appears to extend down the vertical sides of the cylinder.

Stress Von Mises (Pa)
0   25000   50000
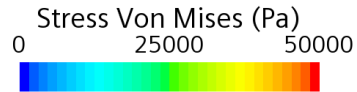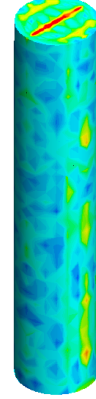
Solution Time 2.5 (s)

(b) High-stress lines have appeared in the cross-section at $t_{\mathrm{solution}} = 2.5$ s perpendicular to the preferential direction of the material. A few higher-stress lines also appear parallel to the cylinder's height along the vertical faces.

Stress Von Mises (Pa)
0   25000   50000
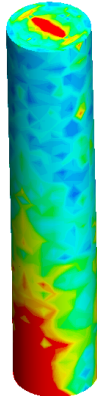
Solution Time 3.75 (s)

(c) A large high-stress area has been created in line with the preferential axis at $t_{\mathrm{solution}} = 3.75$ s, as well as a significant concentration of stress near the base of the cylinder on both the inlet-facing and outlet-facing surfaces of the cylinder.

Stress Von Mises (Pa)
0   25000   50000
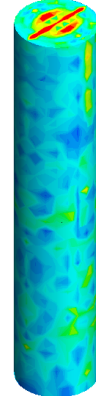
Solution Time 5 (s)

(d) Multiple lines appear in the top face's von Mises stress at $t_{\mathrm{solution}} = 5$ s. Clearly-defined patterns are largely absent on the vertical cylindrical face of the cylinder.

Figure 27: Defomation and von Mises stresses in the anisotropic 5:1 cylinder (no scaling has been applied).

43

VI Conclusions

As anticipated, the clarity and stability of the low-speed fluid flow's wake is diminished substantially when deformable structures are used in place of rigid walls to define the fluid domain.

For taller cylinders such as the 5:1 examples tested, the bending in the structure can act as a spring-damper system with respect to the fluid load. Even when the transients fade, the cylinder continues to oscillate, meaning the traction loads from a fluid could be cause for concern when designing mechanisms with fatigue life in mind. Additionally, increased height offers the opportunity for more complex three-dimensional vortex streets to form in the wake of the cylinder.

The introduction of softer materials allows the structure to deform more easily, while increasing the high frequency content in the wake and lift plots. Softer materials also allow for more unusual deformation patterns, especially in the context of shear-dominated loads, where 'bubbling', 'cratering' and 'flowering' behaviors can occur due to fluid-structure interaction.

The application of anisotropic elasticity to fluid-structure interaction has potential engineering applications, as the structure deforms under fluid loads in a manner significantly influenced by the anisotropy. For example, 'bubbling', 'cratering' and 'flowering' deformation modes have been observed with symmetry along the preferential axis of the material.

VI.1 Limitations

One of the main limitations in the current study concerns the chosen outlet boundary condition as the simulations streamlines were not always parallel at the outlet for the chosen domain size. Additionally, the upper fluid domain surface was typically too close to the top of the cylinder. This affected mainly the simulations with the softest and taller cylinders. Finally, the cylinder's mesh in the softer 1:2 cases was too coarse and may require additional refinement to better explore the unusual behaviors present in these cases.

VI.2 Future Work

The behavior of very soft cylinders under shear-dominated loading conditions is poorly understood, particularly when this load is caused by a fluid flow. Further research into this matter could yield intriguing results and outcomes, particularly if nonlinear materials are to be used.

Further exploration of anisotropic elasticity as a design concept applied to surfaces intended to interact with fluids could allow for novel solutions to engineering problems faced by society, potentially allowing for low-drag control surfaces that still provide excellent responsiveness, adaptive structures that adjust themselves to best withstand or utilize fluid flows, and valve structures that automatically prevent unwanted flow conditions like backflow or excessive pressurization. Further work is required, likely with far greater computational cost, to determine how best to utilize anisotropic elasticity in the design of flexible and functional components and control structures intended to interact with fluid flows.

Many of the simulations presented here may benefit from further refinement in both the fluid and structural domains. Application of alternate coupling methods, like overset meshes and external finite element solvers, could allow for faster, more accurate, and more stable numerical solutions to the FSI problems studied here. Additionally, use of more powerful computing systems, like a computational cluster, could allow for exploration of FSI problems more complex than those covered in this work, as well as the application of better refined meshes and larger problem domains.

References

[1] S. Turek, J. Hron, and M. Razzaq, "Numerical benchmarking of fluid-structure inter-action between elastic object and laminar incompressible flow," *Universitätsbibliothek Dortmund*, 2010.

[2] M. H. Ramage, H. Burridge, M. Busse-Wicher, G. Fereday, T. Reynolds, D. U. Shah, G. Wu, L. Yu, P. Fleming, D. Densley-Tingley, *et al.*, "The wood from the trees: The use of timber in construction," *Renewable and Sustainable Energy Reviews*, vol. 68, pp. 333–359, 2017.

[3] E. Saberski, S. Orenstein, and Y. Novitsky, "Anisotropic evaluation of synthetic surgical meshes," *Hernia*, vol. 15, no. 1, pp. 47–52, 2011.

[4] D. Balzani, S. Deparis, S. Fausten, D. Forti, A. Heinlein, A. Klawonn, A. Quarteroni, O. Rheinbach, and J. Schröder, *Aspects of arterial wall simulations: Nonlinear anisotropic material models and fluid structure interaction*. TU Bergakademie, Fakultät für Mathematik und Informatik, 2014.

[5] B. N. Cox and G. Flanagan, "Handbook of analytical methods for textile composites," 1997.

[6] M. Schäfer, S. Turek, F. Durst, E. Krause, and R. Rannacher, "Benchmark computations of laminar flow around a cylinder," in *Flow simulation with high-performance computers II*, pp. 547–566, Springer, 1996.

[7] S. CD-adapco, "Star ccm+ user guide version 12.04," *CD-Adapco: New York, NY, USA*, 2017.

[8] R. Biswas and R. C. Strawn, "Tetrahedral and hexahedral mesh adaptation for cfd problems," *Applied Numerical Mathematics*, vol. 26, no. 1, pp. 135–151, 1998.

[9] D. Fontes, J. Decker, C. Cole, L. E. Perotti, and M. Kinzel, *An Evaluation of the Fluid Dynamics Character for an Elastically Supported Cylinder in Crossflow (proceedings of ASME 2020 Fluids Engineering Division Summer Meeting)*, p. 1–9. ASME, 2020.

[10] G. Dazhi and R. Tanner, "The drag on a sphere in a power-law fluid," *Journal of non-newtonian fluid mechanics*, vol. 17, no. 1, pp. 1–12, 1985.

[11] S. Dennis and G.-Z. Chang, "Numerical solutions for steady flow past a circular cylinder at reynolds numbers up to 100," *Journal of Fluid Mechanics*, vol. 42, no. 3, pp. 471–489, 1970.

[12] B. Rajani, A. Kandasamy, and S. Majumdar, "Numerical simulation of laminar flow past a circular cylinder," *Applied Mathematical Modelling*, vol. 33, no. 3, pp. 1228–1247, 2009.

[13] S. D'Alessio and J. Pascal, "Steady flow of a power-law fluid past a cylinder," *Acta Mechanica*, vol. 117, no. 1, pp. 87–100, 1996.

[14] A. Roshko, "Experiments on the flow past a circular cylinder at very high reynolds number," *Journal of fluid mechanics*, vol. 10, no. 3, pp. 345–356, 1961.

[15] C. Norberg, "An experimental investigation of the flow around a circular cylinder: influence of aspect ratio," *Journal of Fluid Mechanics*, vol. 258, pp. 287–316, 1994.

[16] R. C. Hibbeler and K. B. Yap, *Mechanics of Materials*. Pearson Education., 10 ed., 2018.

[17] L. E. Perotti, R. Deiterding, K. Inaba, J. Shepherd, and M. Ortiz, "Elastic response of water-filled fiber composite tubes under shock wave loading," *International Journal of Solids and Structures*, vol. 50, no. 3-4, pp. 473–486, 2013.

[18] S.-Y. Fu, B. Lauke, E. Mäder, C.-Y. Yue, and X. Hu, "Tensile properties of short-glass-fiber- and short-carbon-fiber-reinforced polypropylene composites," *Composites Part A: Applied Science and Manufacturing*, vol. 31, no. 10, pp. 1117–1125, 2000.

[19] W. Sun, W. Mao, and B. E. Griffith, "Computer modeling and simulation of heart valve function and intervention," in *Principles of Heart Valve Engineering*, pp. 177–211, Elsevier, 2019.

[20] Dassault Systemes Contributors, "Abaqus." Online (retrieved 30 July 2020), 2020.

[21] A. Joly, S. Etienne, and D. Pelletier, "Galloping of square cylinders in cross-flow at low reynolds numbers," *Journal of Fluids and Structures*, vol. 28, pp. 232–243, 2012.

[22] W. Xu, C. Ji, H. Sun, W. Ding, and M. M. Bernitsas, "Flow-induced vibration of two elastically mounted tandem cylinders in cross-flow at subcritical reynolds numbers," *Ocean Engineering*, vol. 173, pp. 375–387, 2019.

[23] W. Chen, C. Ji, J. Williams, D. Xu, L. Yang, and Y. Cui, "Vortex-induced vibrations of three tandem cylinders in laminar cross-flow: Vibration response and galloping mechanism," *Journal of Fluids and Structures*, vol. 78, pp. 215–238, 2018.

[24] C. Norberg, "Flow around a circular cylinder: aspects of fluctuating lift," *Journal of fluids and structures*, vol. 15, no. 3-4, pp. 459–469, 2001.

[25] R. Kiran, C. Teodoriu, Y. Dadmohammadi, R. Nygaard, D. Wood, M. Mokhtari, and S. Salehi, "Identification and evaluation of well integrity and causes of failure of well integrity barriers (a review)," *Journal of Natural Gas Science and Engineering*, vol. 45, pp. 511–526, 2017.

[26] C. E. Tansley and D. P. Marshall, "Flow past a cylinder on a β plane, with application to gulf stream separation and the antarctic circumpolar current," *Journal of Physical Oceanography*, vol. 31, no. 11, pp. 3274–3283, 2001.

[27] S. Turek and J. Hron, "Proposal for numerical benchmarking of fluid-structure interaction between an elastic object and laminar incompressible flow," in *Fluid-structure interaction*, pp. 371–385, Springer, 2006.

[28] G. De Nayer and M. Breuer, "Numerical fsi investigation based on les: Flow past a cylinder with a flexible splitter plate involving large deformations (fsi-pfs-2a)," *International Journal of Heat and Fluid Flow*, vol. 50, pp. 300–315, 2014.

[29] M. J. Brazell, J. Sitaraman, and D. J. Mavriplis, "An overset mesh approach for 3d mixed element high-order discretizations," *Journal of Computational Physics*, vol. 322, pp. 33–51, 2016.

[30] S. T. Miller, R. Campbell, C. Elsworth, J. Pitt, and D. Boger, "An overset grid method for fluid-structure interaction," *World Journal of Mechanics*, vol. 2014, 2014.

[31] P. Le Tallec and J. Mouro, "Fluid structure interaction with large structural displacements," *Computer methods in applied mechanics and engineering*, vol. 190, no. 24-25, pp. 3039–3067, 2001.

[32] CD-adapco, "Star-CCM+." Online (retrieved 10 August 2020), 2020.